bioRxiv preprint doi: https://doi.org/10.1101/2020.02.05.936237; this version posted February 6, 2020. The copyright holder for this preprint (which was not certified by peer review) is the author/funder. All rights reserved. No reuse allowed without permission.

Bud23 promotes the progression of the Small Subunit Processome to the pre-40S ribosome in *Saccharomyces cerevisiae*

Joshua J. Black[1], Richa Sardana[1, †], Ezzeddine W. Elmir[1], Arlen W. Johnson[1,*]

[1] Department of Molecular Biosciences, The University of Texas at Austin, Austin, Texas, United States of America

[†] Current Address: Department of Molecular Biology and Genetics, Weill Institute for Cell and Molecular Biology, Cornell University, Ithaca, NY

Running tittle: The role of Bud23 in 40S maturation.

*Corresponding author

Email: arlen@austin.utexas.edu (AWJ)

bioRxiv preprint doi: https://doi.org/10.1101/2020.02.05.936237; this version posted February 6, 2020. The copyright holder for this preprint (which was not certified by peer review) is the author/funder. All rights reserved. No reuse allowed without permission.

Abstract

The Small Subunit Processome is a metastable complex that is thought to represent an early checkpoint in the ribosomal small subunit (SSU) assembly pathway. Progression of the SSU Processome towards a mature state involves dynamic rearrangements of RNAs and proteins, but what drives this progression is not known. Previous studies have suggested that the methyltransferase Bud23 acts during SSU Processome progression. Here, we carried out a comprehensive genetic screen that identified bypass suppressors of *bud23*Δ and link Bud23 to a network of physical interactions that stabilize the SSU Processome. Moreover, two of these factors, the RNA helicase Dhr1 and the EF-Tu-like GTPase Bms1, are thought to facilitate crucial structural rearrangements. We propose a model in which Bud23 binding to the 3'-domain promotes the release of factors surrounding its binding site to drive rearrangements during the progression of the SSU Processome.

Introduction

Ribosomes are the molecular machines responsible for translation of the genetic code. They are produced by an energetically expensive and dynamic assembly pathway requiring more than 200 biogenesis factors in eukaryotic cells (reviewed in (Baßler and Hurt, 2019; Klinge and Woolford, 2019; Sloan et al., 2016; Tomecki et al., 2017)). In *Saccharomyces cerevisiae*, the large subunit (LSU, 60S) contains three rRNAs (25S, 5.8S and 5S) and 46 ribosomal proteins (r-proteins), whereas the small subunit (SSU, 40S) has the 18S rRNA and 33 r-proteins (Ben-Shem et al., 2011). Ribosome assembly begins in the nucleolus with the synthesis of the primary rRNA transcript

bioRxiv preprint doi: https://doi.org/10.1101/2020.02.05.936237; this version posted February 6, 2020. The copyright holder for this preprint (which was not certified by peer review) is the author/funder. All rights reserved. No reuse allowed without permission.

(35S in yeast). Co-transcriptional folding of the rRNA is promoted by the recruitment of early ribosomal proteins and biogenesis factors that also process the rRNA. The primary transcript contains the 18S, 5.8S, and 25S rRNAs and four spacer regions that are removed during ribosome assembly: two external transcribed spacers (ETS) and two internal transcribed spacers (ITS) (Fig. S1). Because the 18S rRNA is encoded in the 5'-portion of the primary transcript, which is transcribed first, the initial folding of the pre-rRNA transcript is dedicated to small subunit assembly. Endonucleolytic cleavage within ITS1 separates the SSU precursor from the LSU precursor allowing the subunits to follow independent paths as they undergo further maturation and nuclear export.

The recruitment of biogenesis factors follows a hierarchical order reliant on the formation of secondary, tertiary, and quaternary structure of the pre-ribosomes (Chaker-Margot et al., 2015; Chen et al., 2017; Cheng et al., 2019; Hunziker et al., 2019; Zhang et al., 2016). Nucleolar assembly events of the SSU culminate in completion of the SSU Processome (sometimes referred to as a 90S pre-ribosome), a metastable 6 MDa-sized particle containing the 5' ETS, nascent 18S rRNA, 15 r-proteins, and about 50 biogenesis factors (reviewed in (Barandun et al., 2018; Chaker-Margot, 2018)). During its assembly, the 5', central, 3' major, and 3' minor domains of the 18S rRNA (Fig. S2) fold largely independently (Barandun et al., 2017; Cheng et al., 2019, 2017; Hunziker et al., 2019; Sun et al., 2017). In the assembled SSU Processome, these RNA domains are scaffolded by a multitude of biogenesis factors, the 5' ETS ribonucleoprotein complex (RNP), and U3 snoRNA that prevent their early collapse into the more densely packed structure of the subsequent pre-40S and mature 40S particles. The transition of the SSU Processome to the pre-40S requires several endonucleolytic cleavages of rRNA, release of the 5' ETS RNP and U3, most

bioRxiv preprint doi: https://doi.org/10.1101/2020.02.05.936237; this version posted February 6, 2020. The copyright holder for this preprint (which was not certified by peer review) is the author/funder. All rights reserved. No reuse allowed without permission.

of the SSU Processome factors, and large architectural rearrangements. These events likely coincide with release of the pre-40S into the nucleoplasm. Although recent structural and molecular analysis of the SSU Processome and assembly intermediates have brought assembly of the SSU Processome into focus, there is a dearth of understanding about the events and mechanisms driving the transition of the SSU Processome into a pre-40S particle.

Early recruitment of the U3 snoRNA is crucial for the formation and function of the SSU Processome (Dragon et al., 2002; Hunziker et al., 2016; Zhang et al., 2016). Structural analyses of the SSU Processome show that the box C/D U3 snoRNA threads into the core of the complex where it spatially separates the rRNA domains and scaffolds biogenesis factors (Barandun et al., 2017; Cheng et al., 2017). Two regions of U3, referred to as the 5' and 3' hinges, hybridize to the 5' ETS RNA while its Box A' and Box A regions hybridize to the pre-18S rRNA, henceforth U3-18S heteroduplexes. Notably, Box A hybridizes with the extreme 5'-end of 18S, precluding formation of helix 1 and the Central Pseudoknot (CPK) of the mature 40S particle (Barandun et al., 2017; Sun et al., 2017). The CPK is a universally conserved feature of the SSU formed by long-range, non-canonical base-pairing between helices 1 and 2 that allows the four rRNA domains to compact onto one another (Fig. S2), and generates the environment necessary to establish the decoding center (Ben-Shem et al., 2011; Noeske et al., 2015). Because U3 blocks CPK formation, the release of U3 is a critical, irreversible step in the maturation of the SSU (Chaker-Margot, 2018; Kressler et al., 2017). The unwinding of U3 is catalyzed by the DEAH/RHA helicase Dhr1 (Sardana et al., 2015) which is activated by the SSU Processome factor Utp14 (Boneberg et al., 2019; Roychowdhury et al., 2019; Zhu et al., 2016). Mutational analysis identified a short loop of Utp14 that is necessary and sufficient for the activation of Dhr1 *in vitro* (Boneberg et al., 2019; Zhu et

bioRxiv preprint doi: https://doi.org/10.1101/2020.02.05.936237; this version posted February 6, 2020. The copyright holder for this preprint (which was not certified by peer review) is the author/funder. All rights reserved. No reuse allowed without permission.

al., 2016), and deletion of this loop phenocopies a catalytic *dhr1* mutant *in vivo* (Zhu et al., 2016). How Utp14 times the activation of Dhr1 remains unknown, and neither Dhr1 nor the activation loop of Utp14 have been resolved in SSU Processome structures (Barandun et al., 2017; Cheng et al., 2017). RNA crosslinking and structural analysis indicate that Utp14 binds simultaneously to the 5' ETS RNA, the 5'-, Central, and 3'-ends of the pre-18S rRNA, and to U3, suggesting that Utp14 is uniquely positioned to time Dhr1 activation by monitoring completion of transcription of the small subunit RNA (Barandun et al., 2017; Black et al., 2018; Cheng et al., 2017).

Endonucleolytic cleavages within the rRNA are critical for 40S assembly and conceivably could provide the irreversible step that initiates the transition of the SSU Processome to pre-40S. The current SSU Processome structures all contain rRNA cleaved at A0 but not at A1, indicating that A0 cleavage alone is not sufficient to trigger progression from the SSU Processome (Barandun et al., 2017; Cheng et al., 2019, 2017; Sun et al., 2017). Around the time of Dhr1 function, cleavages at sites A1 within 5' ETS and the site A2 within ITS1 occur (Colley et al., 2000; Sardana et al., 2015). It is possible that cleavage at A1 sets the transition in motion. Site A1 is cleaved by Utp24 which is positioned in the vicinity of site A1. It has been proposed that the essential GTPase Bms1 acts as a molecular switch to drive structural rearrangements needed for Utp24 to access its substrate (Cheng et al., 2017; Wells et al., 2016), but what signals Bms1 activation is not known. Subsequent cleavage at A2 separates the SSU precursor from the LSU precursor. When cleavage at site A2 is inhibited, cleavage at the downstream site A3 can be used instead.

Bud23 is a Trm112-dependent methyltransferase that modifies guanosine 1575 (G1575) within the 3' major domain of 18S rRNA (Létoquart et al., 2014; Sardana and Johnson, 2012;

bioRxiv preprint doi: https://doi.org/10.1101/2020.02.05.936237; this version posted February 6, 2020. The copyright holder for this preprint (which was not certified by peer review) is the author/funder. All rights reserved. No reuse allowed without permission.

White et al., 2008). *BUD23* is a nonessential gene in yeast, but its deletion (*bud23*Δ) causes a significant growth defect that correlates with an approximate 70% reduction of 40S subunits (White et al., 2008). Catalytically inactive *bud23* mutants fully complement the growth defect of *bud23*Δ cells suggesting that the presence of the protein but not its methyltransferase activity is needed for ribosome assembly (Létoquart et al., 2014; White et al., 2008). Bud23 is not typically annotated as an SSU Processome factor and is not present in the SSU Processome structures. However, Bud23 sediments at the positions of both 90S and 40S in sucrose density gradients and *bud23*Δ cells are defective in A2 site cleavage (Sardana et al., 2013), suggesting a role for Bud23 prior to A2 cleavage. In addition, deletion of *BUD23* shows negative genetic interactions with factors that cleave at A3 (Sardana et al., 2013) and is suppressed by extragenic mutations in the SSU Processome factors *DHR1*, *UTP14*, *UTP2 (NOP14)*, and *IMP4* (Sardana, 2013; Sardana et al., 2014, 2013; Zhu et al., 2016). These results imply that Bud23 enters the 40S biogenesis pathway prior to SSU Processome transition to pre-40S and remains associated with early pre-40S particles. Consistent with these observations, the human ortholog of Bud23, WBSCR22, was recently resolved in a cryo-EM structure of an early human pre-40S particle (Ameismeier et al., 2018). Despite the evidence that Bud23 enters the 40S biogenesis pathway at a point prior to A2 cleavage and before complete disassembly of the SSU Processome, its specific function in the transition of the SSU Processome to pre-40S was not known.

Here, we have carried out a comprehensive genetic analysis of extragenic suppressor mutations of *bud23*Δ and identified a genetic and physical interaction network that connects Bud23 to the disassembly of the SSU Processome. We found novel extragenic mutations in *IMP4*, *RPS28A*, *UTP2*, *UTP14*, *DHR1*, and *BMS1* that acted as bypass suppressors of *bud23*Δ. Recent SSU

bioRxiv preprint doi: https://doi.org/10.1101/2020.02.05.936237; this version posted February 6, 2020. The copyright holder for this preprint (which was not certified by peer review) is the author/funder. All rights reserved. No reuse allowed without permission.

Processome structures provide the context to rationalize how these bypass suppressors disrupt SSU Processome structure and imply a role for Bud23 in SSU Processome disassembly. This revealed a network of genetic and physical connections that are tied to Bud23 function. Bms1, Imp4, and Utp2 all interact with the 3' basal subdomain and have helical extensions that embrace the U3-18S substrate of Dhr1. We found that many of the mutations destabilized protein-protein or protein-RNA interactions connecting the 3' major domain to the U3-18S heteroduplexes. Finally, mass spectrometric and Northern blot analysis of particles isolated in the absence of Bud23 revealed an enrichment of late SSU Processome factors and rRNA species not yet cleaved at sites A1 and A2. Together, our data implies that Bud23 binding induces the disassembly of SSU Processome factors connecting the 3' basal subdomain to the U3-18S duplexes. In turn, this promotes Bms1 and Dhr1 activation to drive SSU Processome progression.

Results

Extragenic suppressors of *bud23*Δ map to SSU Processome factors and connect Bud23 to the U3 snoRNA. Bud23 methylates G1575 in the 3' basal subdomain of the 18S rRNA (Létoquart et al., 2014; White et al., 2008), a region comprised of helices 28, 29, 30 41, 41es10, 42, and 43 (Figs. 1A, 1B, & S2) (Sun et al., 2017). The deletion of *BUD23* severely impairs 40S production and cell growth, yet a catalytically inactive Bud23 fully complements *bud23*Δ (Létoquart et al., 2014; White et al., 2008), suggesting that 40S assembly requires Bud23 binding but not rRNA methylation. The slow growth defect of *bud23*Δ places strong selective pressure on cells for extragenic bypass suppressors. Our lab previously reported suppressing mutations in *DHR1*, *UTP14*, and *UTP2,* all coding for late acting SSU Processome factors (Sardana et al., 2014, 2013;

bioRxiv preprint doi: https://doi.org/10.1101/2020.02.05.936237; this version posted February 6, 2020. The copyright holder for this preprint (which was not certified by peer review) is the author/funder. All rights reserved. No reuse allowed without permission.

Zhu et al., 2016). We also found mutations in *IMP4* encoding an early SSU Processome factor (Sardana, 2013). These results connected Bud23 to the late events of the SSU Processome, but they did not allow us to rationalize a mechanism for Bud23 function. The complete SSU Processome harbors nearly 70 ribosomal proteins and biogenesis factors, and we postulated that mapping the mutations to current high-resolution structures of the SSU Processome would help illuminate the function of Bud23. To expand the coverage, we screened for additional spontaneous suppressors by continuously passaging cultures of *bud23*Δ until they arose. We then amplified and sequenced the *IMP4*, *DHR1*, *UTP14*, and *UTP2* loci from these suppressed strains, and identified additional mutations in these genes. Suppressed strains that did not contain mutations in these genes were subjected to whole-genome sequencing and genome variant analysis. This revealed novel suppressing mutations in *RPS28A*, a ribosomal protein that binds the 3' basal subdomain, and *BMS1*, an essential GTPase of the SSU Processome. Mutations in *RPS28A* and *BMS1* were confirmed by Sanger sequencing and verified as suppressors of *bud23*Δ after reintroducing the mutations into *bud23*Δ cells (data not shown).

Portions of Bms1, Imp4, Rps28, Utp2, and Utp14, but not Dhr1, have been resolved in structures of the SSU Processome (Barandun et al., 2017; Cheng et al., 2017; Sun et al., 2017). Remarkably, Bms1, Imp4, Rps28, and Utp2 all interact directly with the 3' basal subdomain containing the Bud23 binding site (Fig. 1C). These factors appear to contribute to the structural stability of the SSU Processome and form multiple protein-protein and protein-RNA contacts (Fig. 1D). Additionally, Bms1, Imp4, and Utp2 each contain extended alpha-helices that penetrate into the core of the SSU Processome where they embrace the U3 Box A and Box A'-18S duplexes (Fig. 1D). Although Dhr1 is not resolved in any of the SSU Processome structures published to date,

bioRxiv preprint doi: https://doi.org/10.1101/2020.02.05.936237; this version posted February 6, 2020. The copyright holder for this preprint (which was not certified by peer review) is the author/funder. All rights reserved. No reuse allowed without permission.

we previously mapped its binding site on U3 to the 5'-hinge and Box A, immediately upstream of and overlapping the Box A and Box A'-18S duplexes that we identified as the substrate for Dhr1 unwinding (Fig. S3A) (Sardana et al., 2015). Only a few segments of Utp14 are resolved in current SSU Processome structures, but Utp14 can be seen binding to pre-rRNA and U3 snoRNA immediately upstream of the duplexes Dhr1 unwinds (Fig. S3A) (Barandun et al., 2017; Black et al., 2018). Intriguingly, Utp14 and the factors positioned at the 3' basal subdomain bookend the U3-18S heteroduplexes. Thus, Imp4, Utp2, and Bms1 provide a physical linkage between the 3' basal subdomain and the U3-18S heteroduplexes that are unwound by Dhr1.

We identified five novel mutations in *BMS1* and one in *RPS28A* as spontaneous suppressors of *bud23*Δ (Fig. 1E). We also found an additional 15 mutations in *DHR1*, 13 mutations in *IMP4*, two mutations in *UTP14*, and one mutation in *UTP2* that were not isolated in our previous studies. Five additional mutations were identified in *UTP2* using error-prone PCR mutagenesis (discussed below). These observations revealed a network of SSU Processome factors that genetically interact with Bud23 and make multiple physical contacts amongst one another (Fig. 1F). Importantly, this interaction network physically connects the 3' basal subdomain with the U3-18S heteroduplex substrates of Dhr1, suggesting a functional linkage between these two sites. Many of the mutations that we report here and previously (Zhu et al., 2016) are in protein-RNA or protein-protein interfaces where they would appear to weaken interactions within the SSU Processome. Because these mutations bypass the absence of Bud23, we propose that Bud23 binding to the 3' basal subdomain induces the release of factors from this region to promote progression of the SSU Processome to a pre-40S particle. In the following

bioRxiv preprint doi: https://doi.org/10.1101/2020.02.05.936237; this version posted February 6, 2020. The copyright holder for this preprint (which was not certified by peer review) is the author/funder. All rights reserved. No reuse allowed without permission.

197 sections, we consider how the *bud23*Δ bypass suppressor mutations affect the dynamics of the
198 particle.
199
200 **The Imp4 and Rps28A mutations mainly cluster around their interfaces with the 3' basal**
201 **subdomain.** We identified 21 unique mutations in *IMP4* and a single mutation within *RPS28A*
202 that suppressed *bud23*Δ (Fig. 1E). All of these mutations partially restored growth in a *bud23*Δ
203 mutant (Fig. 2A), although the *rps28A-G24D* mutation did not suppress as well as the *imp4*
204 mutations, perhaps because expression of the wild-type paralog *RPS28B* partially masked its
205 suppression phenotype. Imp4 is a component of the heterotrimeric Mpp10-Imp3-Imp4 sub-
206 complex (Lee and Baserga, 1999) which enters the SSU Processome at an early stage of its
207 assembly, during transcription of the 5' ETS (Chaker-Margot et al., 2015; Zhang et al., 2016). The
208 Mpp10 complex may serve as an initial binding platform for several additional SSU Processome
209 factors (Sá-Moura et al., 2017). Recent structures show that Imp4 is positioned in the core of the
210 SSU Processome where its N-terminal domain (NTD) contacts the U3-18S heteroduplexes while
211 its RNA-binding Brix domain is cradled in the concave RNA fold of the 3' basal subdomain (Fig.
212 2B) (Barandun et al., 2017; Cheng et al., 2017; Sun et al., 2017). On the other hand, the ribosomal
213 protein Rps28 binds to the opposite, convex surface of the 3' basal subdomain (Fig. 2B), adjacent
214 to but not occluding the Bud23 binding site (Fig. 2B; marked by G1575) (Ameismeier et al., 2018).
215 The mutations in Imp4 primarily mapped to two regions of the protein (Fig. 2C). Most of
216 the mutations were in the Brix domain of Imp4 at its interface with the 3' basal subdomain RNA,
217 henceforth "rRNA interaction" mutations (Fig. 2C). These included mutations of residues S93,
218 R94, S101, R116, N118, N121, and R146 which are all expected to form hydrogen bonds with the

bioRxiv preprint doi: https://doi.org/10.1101/2020.02.05.936237; this version posted February 6, 2020. The copyright holder for this preprint (which was not certified by peer review) is the author/funder. All rights reserved. No reuse allowed without permission.

219 rRNA (Barandun et al., 2017; Cheng et al., 2017). These mutations likely weaken the affinity of
220 the protein for the rRNA. The single Rps28-G24D mutation maps to its rRNA interface with the 3'
221 basal subdomain. Unlike Imp4, Rps28 is an integral component of the small subunit and remains
222 associated with the mature ribosome. Consequently, it is unlikely that the glycine to aspartate
223 substitution promotes release of Rps28. More likely, this mutation may increase the flexibility of
224 the RNA to facilitate release of Imp4 (Fig. 2C). Five of the mutations in Imp4, in residues D74, Y77,
225 H156, H159 and H208, mapped to an intramolecular domain interface between the core of the
226 protein and the NTD that interacts with the U3 Box A'-18S duplex, henceforth "NTD interaction"
227 mutations (Fig. 2D). The NTD interaction mutations may alter the flexibility of the NTD, thereby
228 destabilizing its interaction with the U3 Box A'-18S duplex. The observation that *imp4* mutations
229 that suppress *bud23*Δ are predicted to weaken the affinity of Imp4 for the 3' basal subdomain,
230 suggests that Bud23 binding to the 3' basal subdomain leads to disruption of the protein-RNA
231 interactions in this region.

232 Bud23 is needed for efficient processing at the A2 cleavage site (White et al., 2008). To
233 ask if the suppressing mutations in *IMP4* and *RPS28A* bypass this rRNA processing defect in
234 *bud23*Δ cells, we prepared total RNA from actively dividing wild-type (WT) cells or *bud23*Δ cells
235 with or without a suppressing mutation in *IMP4* or *RPS28A* and probed for rRNA processing
236 intermediates by Northern blotting (Fig. 2E). As we reported previously (Sardana et al., 2013),
237 *bud23*Δ cells showed a loss of the 27SA2 rRNA intermediate, indicating loss of A2 cleavage, and
238 reduced levels of 18S rRNA compared to WT cells, but no concurrent accumulation of 23S rRNAs.
239 Suppression of *bud23*Δ by the *imp4* and *rps28A* mutants partially restored levels of the 27SA2
240 rRNA intermediate and 18S rRNA indicating a restoration of cleavage at site A2 and 40S

bioRxiv preprint doi: https://doi.org/10.1101/2020.02.05.936237; this version posted February 6, 2020. The copyright holder for this preprint (which was not certified by peer review) is the author/funder. All rights reserved. No reuse allowed without permission.

biogenesis. Surprisingly, *bud23*Δ cells also slightly accumulated the 22/21S intermediates (Fig. 2E). 22S represents rRNA cleaved at sites A0 and A3 but not A1 or A2 while 21S represents rRNA cleaved at sites A1 and A3 but not A2. (Fig. S1). Although the A2-A3 probe cannot distinguish between the 22S and 21S intermediates the A0-A1 probe gave a similar hybridization signal indicating that the 22S rRNA is responsible for some of this signal (Fig. 2E). Suppression of *bud23*Δ partially alleviated the accumulation of this species. This was most evident in the strains harboring the *imp4* mutants S93T, R94S, N121I, and H159R. These data indicate that Bud23 affects not only A2 processing, as we previously reported (White et al., 2008), but also cleavage at A1.

As a complementary approach to ask if *bud23*Δ suppressors restored 40S biogenesis, we analyzed ribosomal subunit levels on sucrose density gradients after separating free ribosomal subunits, 80S, and polysomes from wild-type cells and *bud23*Δ cells with or without a suppressing mutation. In wild-type cells, there was an appreciable steady-state level of free 40S and 60S subunits (Fig. 2F). In contrast, in *bud23*Δ cells in which 40S production is limited, the free 40S peak disappeared and the amount of free 60S was dramatically increased, at the expense of 80S (Fig. 2C). The introduction of suppressing mutations in *imp4* or *rps28a* partially restored the levels 80S and free 40S, similar to the suppression of *bud23*Δ by mutations in *utp14* or *utp2* that we reported previously (Sardana et al., 2013). Taken together, the Northern blotting and sucrose density gradient data indicate that *imp4* and *rps28A* mutants partially alleviate the 40S biogenesis defects of *bud23*Δ cells.

bioRxiv preprint doi: https://doi.org/10.1101/2020.02.05.936237; this version posted February 6, 2020. The copyright holder for this preprint (which was not certified by peer review) is the author/funder. All rights reserved. No reuse allowed without permission.

Utp2 mutants that suppress *bud23*Δ destabilize Utp2 interaction with Imp4. Our lab previously identified *utp2-A2D* as a spontaneous and dominant suppressor of *bud23*Δ that partially restores 40S biogenesis and A2 processing of the primary rRNA transcript (Sardana et al., 2013). From our screen for additional spontaneous suppressors of *bud23*Δ, we found an additional Utp2 mutation, *utp2-L9S*, that suppressed *bud23*Δ (Fig. 3A). Utp2, also known as Nop14, assembles into the SSU Processome with its binding partners Emg1, Noc4, and Utp14 (Baßler et al., 2016; Liu and Thiele, 2001; Vincent et al., 2018), once the 3' minor domain is fully transcribed (Chaker-Margot et al., 2015; Zhang et al., 2016). The association of human Utp2 with human pre-40S complexes indicates that Utp2 remains on nascent particles during the transition from the SSU Processome to pre-40S (Ameismeier et al., 2018) suggesting that it has an active role in particle progression.

To gain further insight into the mechanism by which mutations in *UTP2* suppress *bud23*Δ, we performed random PCR mutagenesis of *UTP2* and identified six additional mutations in *UTP2* that suppressed *bud23*Δ to different degrees (Fig. 3B; left panel). In this screen we also reisolated the previously identified *utp2-A2D* mutation. All mutants fully complemented loss of Utp2 (Fig. 3B; right panel). The suppressing mutations all mapped to the N-terminal domain of Utp2. Four of the mutations clustered around the extreme N-terminus of Utp2 and another three clustered around residues 148-151. In an attempt to generate mutants with stronger phenotypes than the individual mutants, we generated the combinatorial mutants *utp2-DPE* containing the mutations A2D, L6P, and K7E, and *utp2-SSH* harboring the mutations L148S, F149S, and L151H. Both of the combinatorial mutants retained the ability to suppress *bud23*Δ and fully complemented loss of *UTP2*, but *utp2-SSH* was a stronger suppressor than *utp2-DPE* (Fig. 3B).

bioRxiv preprint doi: https://doi.org/10.1101/2020.02.05.936237; this version posted February 6, 2020. The copyright holder for this preprint (which was not certified by peer review) is the author/funder. All rights reserved. No reuse allowed without permission.

Based on recent partial structures of Utp2 within the SSU Processome (Barandun et al., 2017; Cheng et al., 2017) the globular domain of Utp2 directly contacts the Emg1 heterodimer, Enp1, and Noc4 within a region of the 3' major domain that will make up the beak of the mature SSU, while its extended N- and C-terminal arms pierce deep into the core of the SSU Processome. The C-terminal arm of Utp2 contacts the U3 Box A'-18S duplex while its NTD contacts the Brix domain of Imp4 (Figs. 1D & 3C). Notably, the suppressor mutations we identified in Utp2 are within its NTD. Four of the residues (L6, K7, L9 and F58) mutated in our screen were resolved in current structures of the SSU Processome (Fig. 3C). Residues L6, K7, and L9 are within a small helix on the extreme N-terminus of Utp2 that interacts with Imp4, while K7 appears to contact the phosphate backbone of C1623 of the 3' basal subdomain. Meanwhile, F58 of Utp2 makes an additional nearby contact between these proteins. These observations prompted us to speculate that the *utp2* suppressors of *bud23*Δ perturb the interaction between Utp2 and Imp4. Previous large-scale yeast-two hybrid (Y2H) studies did not report an interaction between Utp2 and Imp4 (Baßler et al., 2016; Vincent et al., 2018). However, those studies used Utp2 constructs harboring N-terminal fusions of GAL4 activating or DNA binding domain (AD and BD, respectively). Because the apparent interaction between Utp2 and Imp4 requires the extreme N-terminus of Utp2 (Fig. 3C), such a fusion protein could sterically hinder their interaction. To this end, we cloned a Utp2 Y2H construct harboring an HA-tagged GAL4 activating domain fused to its C-terminus (Utp2-AD-HA), which allowed us to detect an interaction between Utp2-AD-HA and BD-myc-Imp4 (Fig. 3D; left panel). Using this system, we assayed the Utp2-DPE, Utp2-F58S, and Utp2-SSH mutants for their ability to interact with Imp4. All of the mutants showed decreased interaction with Imp4 with the Utp2-F58S and Utp2-SSH mutants being the most severe. All the mutant Utp2 proteins

bioRxiv preprint doi: https://doi.org/10.1101/2020.02.05.936237; this version posted February 6, 2020. The copyright holder for this preprint (which was not certified by peer review) is the author/funder. All rights reserved. No reuse allowed without permission.

306 were expressed to similar levels indicating that the reduced interaction was not due to
307 differences in expression or degradation of the mutant proteins (Fig. 3D; right panel). The results
308 from the analysis of Utp2-DPE and Utp2-F58S are consistent with the notion that the mutations
309 in Utp2 that suppress *bud23*Δ disrupt the interaction between Utp2 and Imp4. The result of Utp2-
310 SSH losing interaction with BD-Imp4 suggests that the flexible, unresolved region of Utp2
311 between R116 and P201 interacts with Imp4, but we cannot rule out the formal possibility that
312 these mutations suppress *bud23*Δ by some other unknown means.

313 F58 of Utp2 fits into a hydrophobic pocket of Imp4 (Fig. 3E; upper panel). Interestingly,
314 two mutations in *IMP4*, V170F and P252L, that suppressed *bud23*Δ (Figs. 2A & 2B) map to
315 residues that line this pocket (Fig. 3E; lower panel). The positions of these two mutations predict
316 that they could also disrupt the interaction between Imp4 and Utp2. To test this possibility, we
317 introduced the V170F and P252L mutations into the BD-myc-Imp4 vector and assayed for their
318 interaction with Utp2-AD-HA. Indeed, mutation of either of these residues caused a loss of
319 interaction between Utp2 and Imp4 (Fig. 3F; upper panel), and the loss of interaction could not
320 be explained by reduced protein expression of the mutant Imp4 constructs (Fig. 3F; lower panel).
321 These results, together with the Y2H assays using mutant Utp2 strongly suggest that disrupting
322 the interaction between Imp4 and Utp2 bypasses the 40S assembly defect in the absence of
323 Bud23.

324

325 **Bms1 mutants that suppress *bud23*Δ are poised to affect the conformational state of Bms1.** We
326 found five *bud23*Δ-suppressing mutations within *BMS1* (Figs. 1F & 4A). Like the mutations in
327 *DHR1*, *UTP14*, *UTP2*, *IMP4*, and *RPS28A* (Fig. 2E) (Sardana et al., 2014, 2013; Zhu et al., 2016),

bioRxiv preprint doi: https://doi.org/10.1101/2020.02.05.936237; this version posted February 6, 2020. The copyright holder for this preprint (which was not certified by peer review) is the author/funder. All rights reserved. No reuse allowed without permission.

mutant *bms1* alleles partially alleviated the rRNA processing defects and restored 40S biogenesis (Figs. 4B & 4C) suggesting that these mutations overcome the same biogenesis defect in the absence of Bud23 that the other *bud23*Δ suppressors do. *BMS1* encodes a 136 kDa GTPase that is essential for 40S biogenesis (Gelperin et al., 2001; Wegierski et al., 2001). Bms1 forms a subcomplex with Rcl1 (Delprato et al., 2014; Gelperin et al., 2001; Karbstein et al., 2005; Karbstein and Doudna, 2006) prior to its entry into the SSU Processome after completion of the 3' minor domain (Chaker-Margot et al., 2015; Zhang et al., 2016). The GTPase activity of Bms1 has been confirmed *in vitro* (Karbstein et al., 2005; Karbstein and Doudna, 2006), and its ability to bind GTP is essential (Delprato et al., 2014) suggesting that it is a functional GTPase *in vivo*. However, the specific role of Bms1 within the SSU Processome has not been well explored. GTPases often serve as molecular switches that undergo conformational changes (reviewed in (Wittinghofer and Vetter, 2011)). Due to its position in the SSU Processome, it has been suggested that Bms1 helps remodel the SSU Processome core so the endonuclease Utp24 can access and cleave the A1-site (Cheng et al., 2017). Thus, this model predicts that Bms1 has a role in the progression of the SSU Processome to the pre-40S.

More than half of Bms1 has been resolved in structures of the SSU Processome and can be divided into five major domains and two small regions that bind its partner Rcl1 and the acetyltransferase Kre33 (Fig. 4D) (Barandun et al., 2017; Cheng et al., 2017; Sun et al., 2017). Domain I contains the GTPase catalytic site and, together with the beta-barrels of domains II and III, forms a globular body. Domain IV protrudes from this globular body to interact with the 3' basal subdomain RNA and contacts the CTDs of Imp4 and Utp2 (Fig. 4E). Finally, the C-terminal domain V begins as an extended strand that lays on domain III before becoming an extended

bioRxiv preprint doi: https://doi.org/10.1101/2020.02.05.936237; this version posted February 6, 2020. The copyright holder for this preprint (which was not certified by peer review) is the author/funder. All rights reserved. No reuse allowed without permission.

alpha-helix that inserts between the U3 Box A'-18S and U3 Box A-18S heteroduplexes (Fig. 4D). Although the five mutations that suppressed *bud23*Δ map to domains I, II, III and V (Fig. 4D; upper panel) , in 3D structure the mutated residues D124, D843, A903, and S1020 lie immediately under the unstructured strand connecting domain IV to the extended C-terminus (Fig. 4F). Thus, four of the five suppressing mutations likely promote the flexibility of this connecting loop. G813 is located in the connector between Domains II and III where it could alter the relative positioning of these two domains and influence how domain III interacts with the unstructured strand of domain V.

Bms1 is structurally related to the translation elongation factor EF-Tu which delivers amino-acyl tRNAs to the ribosome (Fig. S4A) (Wegierski et al., 2001). Comparison of the Bms1 structure from the SSU Processome to the crystal structures of EF-Tu bound to GDP or the non-hydrolysable GTP analog, GDPNP, suggests that Bms1 is in the GTP-bound state in the SSU Processome structures and allows us to speculate how Bms1 functions. The beta-barrels of domains II and III of Bms1 are conserved in EF-Tu (Fig. S4B). In the GTP-bound state, the beta-barrels of EF-Tu are positioned to accommodate tRNA binding (Fig. S4C) (Nissen et al., 1999). In GDP-bound EF-Tu the beta-barrels are rotated to promote tRNA release (Figs. S4C & S4D) (Song et al., 1999). Interestingly, the comparison of the EF-Tu and Bms1 structures revealed that the space occupied by tRNA in EF-Tu (Fig. S4E) is occupied by an N-terminal helix of Mpp10 and the unstructured strand of Bms1 that connects domain IV to the extended C-terminus that interacts with U3 (Fig. S4F). This observation suggests that the GTP hydrolysis-induced conformational changes of Bms1 could facilitate undocking of the unstructured strand of Bms1 and Mpp10 from the conserved core of Bms1. Notably, four of the five mutations in *BMS1* that suppressed *bud23*Δ

bioRxiv preprint doi: https://doi.org/10.1101/2020.02.05.936237; this version posted February 6, 2020. The copyright holder for this preprint (which was not certified by peer review) is the author/funder. All rights reserved. No reuse allowed without permission.

were either within or contact this strand of Bms1 (Fig. S4F). We suggest that these mutations facilitate release of this strand and, perhaps, Mpp10 from Bms1.

Disruption of Dhr1 and Utp14 interaction suppresses *bud23*Δ. Our lab previously reported 10 mutations in *DHR1* that suppress *bud23*Δ (Sardana et al., 2014). Here, we isolated an additional 15 suppressing mutations within *DHR1* (Figs. 1F & 5A). Dhr1 is the DEAH-box RNA helicase responsible for unwinding the U3 snoRNA from the SSU Processome (Colley et al., 2000; Sardana et al., 2015). The protein harbors a conserved helicase core containing two RecA domains, a Winged-helix (WH) domain, a Helical Bundle (HB) domain, and an OB-fold domain (Fig. 5A). Dhr1 also contains an N-terminal domain (NTD) that interacts with Bud23 (Létoquart et al., 2014; Sardana et al., 2014) and a unique C-terminal domain (CTD) that enhances its interaction with its activator Utp14 (Boneberg et al., 2019; Roychowdhury et al., 2019; Zhu et al., 2016). Although Dhr1 has yet to be resolved in SSU Processome structures, recent crystal structures of recombinant yeast Dhr1 (Roychowdhury et al., 2019) and its murine homolog DHX37 (Boneberg et al., 2019) lacking the NTD allow us to map most of the mutated residues to structure (Fig. 5B). Consistent with our previous report (Sardana et al., 2014), the overwhelming majority of the mutations map to residues on the surface of the RecA1 and RecA2 domains (Fig. 5C). We previously reported that Utp14, the cofactor of Dhr1, binds the RecA1/2 domains (Zhu et al., 2016). Based on this, we hypothesized that the mutations within the RecA1/2 domains could affect its interaction with Utp14. To this end, we again turned to yeast 2-hybrid analysis between BD-myc-Dhr1 and AD-HA-Utp14. We cloned three constructs that combined several mutations within or proximal to the RecA1 domain (E360K, E397D, E402G, D408Y), within the RecA2 domain

bioRxiv preprint doi: https://doi.org/10.1101/2020.02.05.936237; this version posted February 6, 2020. The copyright holder for this preprint (which was not certified by peer review) is the author/funder. All rights reserved. No reuse allowed without permission.

(H593Y, R596C, E831K), or in both the RecA1 and RecA2 domains (R563M, D566Y, E831K, F837L) in the Y2H Dhr1 construct and tested them for the ability to interact with Utp14. All three mutants showed a significant loss of interaction with Utp14 (Fig. 5D; left). All three of the mutant proteins expressed similarly (Fig. 5D; right), indicating that the loss-of-interaction was not due to differential expression. Thus, we conclude that mutations within the RecA1 and RecA2 of Dhr1 that bypass *bud23*Δ do so by weakening its interaction with Utp14.

Utp14 stimulates the unwinding activity of Dhr1 (Boneberg et al., 2019; Choudhury et al., 2018; Zhu et al., 2016). We previously reported five mutations within Utp14 that suppress the growth defect of *bud23*Δ (Zhu et al., 2016). Notably, these mutations were within a region of Utp14 spanning residues 719 to 780 that interacts with Dhr1 , and extensive mutation or deletion of this region reduced Utp14 interaction with Dhr1 , Utp14-dependent activation of Dhr1 activity *in vitro* and phenocopied catalytically null Dhr1 *in vivo* (Zhu et al., 2016). Here, we report two additional mutations in Utp14, W791L and W794L, that suppressed *bud23*Δ (Fig. S3B). These mutations are slightly downstream of those previously identified and affect two highly conserved tryptophan residues in a motif weakly reminiscent of a G patch, a motif common to activators of DEAH/RHA RNA helicases (Zhu et al., 2016). Unfortunately, these residues are not resolved in the SSU Processome structures, but we suspect that these mutations also weaken the interaction between Utp14 and Dhr1. How mutations that weaken the interaction Utp14-Dhr1 interaction promote progression of the SSU Processome in the absence of Bud23 is intriguing considering that Utp14 activates Dhr1 (Boneberg et al., 2019; Zhu et al., 2016). These results suggest that the nature of Utp14-Dhr1 interaction is more complex than originally thought and will require additional work to understand.

bioRxiv preprint doi: https://doi.org/10.1101/2020.02.05.936237; this version posted February 6, 2020. The copyright holder for this preprint (which was not certified by peer review) is the author/funder. All rights reserved. No reuse allowed without permission.

Bud23 depletion partially inhibits SSU Processome progression. The above genetic results suggest that disrupting protein-protein and protein-RNA interactions in the 3' basal subdomain of the SSU Processome can partially bypass the absence of Bud23. We interpret these results to indicate that Bud23 binding leads to disassembly events that promote the progression of the SSU Processome. To test the idea that Bud23 promotes disassembly events, we characterized pre-ribosomal particles in the absence of Bud23. We introduced a genomically encoded C-terminal Auxin-Induced Degron (AID) tag on Bud23 for rapid depletion of Bud23 upon the addition of the small molecule auxin without the need for shifting carbon sources (Nishimura et al., 2009). The *BUD23-AID* strain grew similar to wild-type cells on media lacking auxin, while it showed a growth defect comparable to the *bud23*Δ strain on media containing auxin indicating that the AID tag is functional and does not significantly impact Bud23 function (Fig. 6A). Bud23-AID was significantly depleted after 10 minutes and was undetectable after two hours of auxin treatment (Fig. 6B). We first asked if Bud23 depletion impacted the association of Imp4 with pre-40S particles. We depleted Bud23 for two hours and separated particles by ultracentrifugation on sucrose density gradients. Western blot analysis across the gradients showed that in wild-type cell extracts Imp4 was present throughout the gradient but showed enrichment in the 40S to 80S fractions and near the top of the gradient (Fig. 6C). The population near the top of the gradient likely reflects its association with the Mpp10 sub-complex (Gallagher and Baserga, 2004; Gérczei and Correll, 2004; Lee and Baserga, 1999) whereas the population at 80S reflects its association with the SSU Processome because U3 snoRNA also sedimented in this position. We also monitored the sedimentation of the biogenesis factor Enp1 harboring a C-terminal Tandem Affinity Purification

bioRxiv preprint doi: https://doi.org/10.1101/2020.02.05.936237; this version posted February 6, 2020. The copyright holder for this preprint (which was not certified by peer review) is the author/funder. All rights reserved. No reuse allowed without permission.

(TAP) tag. In wild-type cells, Enp1-TAP sedimented throughout the gradient indicating its known binding to both the SSU Processome and pre-40S particles, with enrichment at 40S reflecting its steady-state association with pre-40S particles (Schäfer et al., 2003). Upon depletion of Bud23-AID, both Imp4 and Enp1-TAP showed a loss of sedimentation in the 80S region while they maintained or increased sedimentation in the 40S region of the gradient. Surprisingly, U3 snoRNA sedimentation was not obviously affected. These results indicate that both Imp4 and Enp1 remain associated with 40S precursor particles in the absence of Bud23 while their presence in the SSU Processome is depleted.

To further understand the nature of 40S precursors that accumulate in the absence of Bud23, we used Enp1-TAP as a bait for affinity purifications. Enp1-TAP is an ideal bait for these experiments as it binds to the SSU Processome, upstream of Bud23 binding, and is released downstream of Bud23 release (Schäfer et al., 2003). We affinity purified Enp1-TAP particles from WT and Bud23-AID strains after two hours of auxin treatment. Following elution, particles were sedimented through sucrose cushions to separate free Enp1 from preribosome-bound Enp1. The associated proteins were then separated by SDS-PAGE. The depletion of Bud23 lead to the reduction of three major protein species (Fig. 7A; black lines) and the accumulation of seven species (Fig. 7A; blue lines). Mass spectrometry identified the depleted proteins as the pre-40S factors Tsr1, Rio2, and Nob1, while mostly late-acting, SSU Processome factors comprised the accumulated factors. We further analyzed these particles by performing mass spectrometry on the entire samples. To determine the approximate stoichiometry of each protein, we calculated a relative spectral abundance factor (RSAF) for 40S biogenesis proteins by dividing the spectral counts for each protein by its molecular weight then normalizing this value to the bait, Enp1. This

bioRxiv preprint doi: https://doi.org/10.1101/2020.02.05.936237; this version posted February 6, 2020. The copyright holder for this preprint (which was not certified by peer review) is the author/funder. All rights reserved. No reuse allowed without permission.

460 analysis revealed the proteomic compositions of the wild-type and Bud23-depleted particles (Fig.
461 S5 & Supplemental File 1). Although various proteins were accumulated or depleted from these
462 particles, the levels of the proteins that showed genetic interaction with *bud23*Δ remained
463 relatively constant in the absence of Bud23, with the exception of Utp2. We interpret this to
464 indicate that particles are arrested upstream of the release of these factors where they remain
465 stoichiometric with Enp1, the bait protein. To simplify our analysis, we calculated a log2-fold
466 change between Bud23-depleted and wild-type particles for each protein and only considered
467 proteins to be significant if they showed a ± 0.5-fold increase or decrease with a difference of 10
468 spectral counts (Fig. S6). This analysis revealed a set of 26 proteins that significantly changed
469 upon Bud23-depletion. These results agreed with what we observed by SDS-PAGE in Fig. 7A in
470 that there was an accumulation of mainly SSU Processome factors and a depletion of mostly pre-
471 40S factors. With the exception of Utp2, the accumulated factors are not localized to the 3' basal
472 subdomain, but several have late roles in the SSU Processome. Recent work suggests that Bfr2,
473 Enp2, Lcp5, and Kre33, which accumulated in the absence of Bud23, help finalize structural
474 compaction of the SSU Processome (Cheng et al., 2019) while Mrd1 may have a role in resolving
475 the U3-5' ETS duplexes (Lackmann et al., 2018). Strikingly, the pre-40S factors Rio1 and Slx9
476 accumulated in the absence of Bud23. While Slx9 functions in the nuclear export of pre-40S
477 particles (Fischer et al., 2015), Rio1 acts during the final cytoplasmic pre-40S maturation steps
478 (Ferreira-Cerca et al., 2014) significantly downstream of the point in which Bud23 acts. These
479 results suggest that in the absence of Bud23, certain regions of the particle have progressed to a
480 pre-40S state whereas other regions appear blocked in their progression.

bioRxiv preprint doi: https://doi.org/10.1101/2020.02.05.936237; this version posted February 6, 2020. The copyright holder for this preprint (which was not certified by peer review) is the author/funder. All rights reserved. No reuse allowed without permission.

We also probed for the rRNA intermediates that co-precipitated with Enp1-TAP in the presence and absence of Bud23 (Fig. 7B). We observed that Enp1 decreased association with the 23S rRNA with a concomitant accumulation of both 21S and 22S RNAs in the absence of Bud23. By quantifying the amount of 22S relative to 35S detected with A0-A1 probe vs the amount of 21S/22S relative to 35S detected with the A2-A3 probe we calculate that the 21S and 22S species are approximately equally abundant in the Enp1-TAP sample from Bud23-depleted cells. The accumulation of 21S and 22S indicates that processing at A2 was inhibited upon Bud23 depletion, as we have previously reported (White et al., 2008). The accumulation of 22S was unexpected as this indicates a defect in A1 cleavage as well. Furthermore, we saw a modest accumulation of the A0-cleaved 5' ETS rRNA (~1.5-fold) and U3 snoRNA (~1.2-fold). Consistent with what is seen in whole cell extracts of *bud23*Δ cells (Figs. 2E & 4B) (Sardana et al., 2014, 2013), we also saw that 27SA2 intermediate was present in the input and IP for the wild-type sample, but totally absent in the Bud23-depleted sample (Fig. 7B). These results reconfirm that Bud23 is needed for efficient processing at A2 and support the possibility that Bud23 also impacts cleavage at A1.

Discussion

Bud23 was initially identified as the methyltransferase that modifies G1575 in 18S rRNA and is thought to act at a relatively late stage in nuclear 40S assembly (White et al., 2008). Although it is conserved from yeast to humans and deletion of *BUD23* in yeast leads to severely impaired growth, its methyltransferase activity is dispensable for ribosome assembly (White et al., 2008; Zorbas et al., 2015). This indicates that the primary function of Bud23 stems from its binding to 40S precursors. A recent structure of human Bud23 on pre-40S (Ameismeier et al., 2018) and the lack of a requirement for Bud23 in assembly of the SSU Processome are consistent

bioRxiv preprint doi: https://doi.org/10.1101/2020.02.05.936237; this version posted February 6, 2020. The copyright holder for this preprint (which was not certified by peer review) is the author/funder. All rights reserved. No reuse allowed without permission.

503 with the notion that Bud23 acts late in the nuclear assembly pathway. Nevertheless, there have
504 been hints that Bud23 acts earlier than pre-40S. Notably, we previously reported that mutations
505 in the RNA helicase Dhr1, its activator Utp14, Utp2, and Imp4, all canonical SSU Processome
506 factors, suppress the growth defect of *bud23*Δ cells (Sardana, 2013; Sardana et al., 2014, 2013;
507 Zhu et al., 2016). Because Dhr1 is the RNA helicase that unwinds U3 snoRNA from 18S rRNA
508 (Sardana et al., 2015), a critical event during the remodeling of the SSU Processome to pre-40S,
509 the functional interaction between Bud23 and Dhr1 suggests a role for Bud23 during this
510 remodeling event. Here, we have provided a significant body of additional evidence to build a
511 case for Bud23 having a direct role in the transition of the SSU Processome to pre-40S.

512 The majority of mutations that we found as suppressors of *bud23*Δ were in Imp4 and Dhr1
513 with additional mutations in Bms1, Rps28A, Utp2, and Utp14. The Imp4 mutations clustered
514 primarily in its interface with the 3' basal subdomain of rRNA opposite the binding site of Bud23
515 and are predicted to be disrupting interactions (Fig. 2C). The Brix domain of Imp4 and the NTD of
516 Utp2 contact one another (Fig. 3C), and we showed that suppressing mutations on either side of
517 the Imp4-Utp2 interface disrupted the interaction between these proteins (Figs. 3D & 3F).
518 Furthermore, many of the suppressing mutations in Dhr1 disrupted its interaction with it binding
519 partner Utp14 (Fig. 5D). Lastly, mutations in Bms1 that may promote a conformational change
520 within Bms1 were also identified as *bud23*Δ suppressors (Fig. 4F). The picture that emerges from
521 this extensive network of genetic and physical interactions is that the absence of Bud23 can be
522 bypassed by disrupting protein-protein and protein-RNA contacts that appear to be important
523 for the structure of the SSU Processome. We also determined the proteomic and RNA
524 composition of 40S precursors purified in the absence of Bud23 (Fig. 7). We observed an

bioRxiv preprint doi: https://doi.org/10.1101/2020.02.05.936237; this version posted February 6, 2020. The copyright holder for this preprint (which was not certified by peer review) is the author/funder. All rights reserved. No reuse allowed without permission.

accumulation of late SSU Processome factors and inefficiently processed rRNAs and the depletion of pre-40S factors. This atypical progression of the SSU Processome further underscores the role of Bud23 in the transition of the particle to the pre-40S. Thus, we propose that Bud23 binding to the 3' basal subdomain promotes remodeling of this region of the SSU Processome during its transition to the pre-40S particle. In the absence of Bud23, mutations that destabilize this region of the SSU Processome can suffice to promote this transition.

The network of genetic and physical interactions that we define in this work link Bud23 to the functions of Dhr1 and Bms1. These two enzymes are thought to drive structural rearrangements critical to the transition of the SSU Processome to a pre-40S particle. Dhr1 catalyzes U3 snoRNA removal (Sardana et al., 2015), while Bms1 may remodel RNA to allow A1 cleavage (Cheng et al., 2017). The requirement of Dhr1 and Bms1 in disassembly of the SSU Processome is reminiscent of the relationship between the DExH RNA helicase Brr2 and the EF-G-like GTPase Snu114 that regulate Spliceosome disassembly (Small et al., 2006). In the case of the spliceosome, it is believed that nucleotide-dependent conformational changes in Snu114 activate Brr2, mediated through the C-terminus of Snu114. It is possible that the actions of Dhr1 and Bms1 are similarly coordinated. Bms1 has a globular GTPase domain composed of domains I-III that binds helices 15-18 of the 5'-domain of 18S rRNA while domain IV binds to the 3' basal subdomain. A long C-terminal helix of Bms1 extends into the SSU Processome and wedges between the U3 Boxes A and A' heteroduplexes with 18S rRNA (Figs. 1D & S3A), the substrates of Dhr1. In this way, Bms1 and Dhr1 can be directly linked mechanistically. We previously mapped the binding site of Dhr1 to U3 snoRNA immediately downstream of the Boxes A and A' heteroduplexes (Sardana et al., 2015). As Dhr1 is a DExH-box helicase it likely translocates in a 3'

bioRxiv preprint doi: https://doi.org/10.1101/2020.02.05.936237; this version posted February 6, 2020. The copyright holder for this preprint (which was not certified by peer review) is the author/funder. All rights reserved. No reuse allowed without permission.

to 5' manner (Boneberg et al., 2019) and would be poised to disrupt the U3 heteroduplexes. However, the helical extension of Bms1 with those of Utp2 and Imp4 could act as obstructions to control Dhr1 translocation.

The functional links of Bud23 with Bms1 and Dhr1 suggest that it may coordinate their activates. We suggest two possible mechanisms in which Bud23 binding facilitates SSU Processome progression. Following Utp14-dependent recruitment of Dhr1 (Black et al., 2018; Zhu et al., 2016), Dhr1 is positioned upstream of the U3-18S heteroduplexes where it is primed for activation, but the helical extensions of Bms1, Imp4, and Utp2 that embrace its substrate prevent Dhr1 access. (Fig. 8A). After completion of the SSU Processome, Bud23 binding to the 3' basal subdomain signals the GTPase activity of Bms1 (Fig. 8B). Subsequently, Bms1 drives structural rearrangements to displace the helical extensions allowing Dhr1 to progress forward through its substrate. Alternatively, Dhr1 could initiate unwinding of the U3 Box A-18S duplex until it runs into the helical extensions of Bms1, Imp4, and Utp2 where they act as a physical barrier (Fig. 8C). At this point, entry of Bud23 into the particle induces Bms1 activation. Subsequent removal of the helices would allow Dhr1 to translocate through the U3 Box A'-18S duplex. Additional biochemical and structural work will be needed to determine if either of these models is correct.

While our data indicate that Bud23 binding assists in the progression of the SSU Processome, how Bud23 binding is transduced to Bms1 or Dhr1 in unclear. Bud23 could promote transition by one of several different and not mutually exclusive means. The binding of Bud23 could alter the structure of the 3' basal subdomain RNA, facilitating the release of factors. However, we note that the structure of the 3' basal subdomain RNA remains virtually unchanged between the SSU Processome structure and the Bud23-bound pre-40S. This suggests that Bud23

bioRxiv preprint doi: https://doi.org/10.1101/2020.02.05.936237; this version posted February 6, 2020. The copyright holder for this preprint (which was not certified by peer review) is the author/funder. All rights reserved. No reuse allowed without permission.

569 binding does not directly alter the RNA structure to promote release of Imp4 and associated
570 factors. In the SSU Processome structures, the future binding site of Bud23 is occupied by the
571 methyltransferase Emg1 (Barandun et al., 2017; Cheng et al., 2017; Sun et al., 2017). It is possible
572 that Bud23 is needed for the release of Emg1 to set in motion disassembly of factors from the 3'
573 basal subdomain. This model predicts that Emg1 would accumulate on particles upon Bud23
574 depletion, a result that we did not observe (Figs. 7A & S6).

575 Furthermore, an additional consideration that must be made is that *BUD23* is not
576 essential. One would expect that if Bud23 binding to the SSU Processome was absolutely required
577 for its progression that Bud23 would be essential. Deletion of Bud23 causes a roughly 70%
578 reduction in 40S relative to 60S (White et al., 2008), suggesting that Bud23 is needed to produce
579 the majority of 40S. Interestingly, roughly 70% of rRNA processing occurs co-transcriptionally
580 with the remaining 30% occurring post-transcriptionally (Kos and Tollervey, 2010). Cleavage at
581 the A2 site appears to reflect co-transcriptional processing while cleavage at the A3 site is
582 observed in post-transcriptional processing. Thus, the post-transcriptional pathway may be the
583 primary processing pathway used in *bud23*Δ mutants. Consistent with this idea, *bud23*Δ shows a
584 strong negative genetic interaction with components of the RNase MRP complex responsible for
585 processing A3 (Sardana et al., 2013). This suggests that the progression of the SSU Processome
586 in the post-transcriptional pathway follows a Bud23-independent mechanism that differs from
587 the model that we have proposed in this study. Because the functions of Bms1 and Dhr1 are
588 indispensable such an alternative mechanism most likely still requires their enzymatic activities.
589

bioRxiv preprint doi: https://doi.org/10.1101/2020.02.05.936237; this version posted February 6, 2020. The copyright holder for this preprint (which was not certified by peer review) is the author/funder. All rights reserved. No reuse allowed without permission.

Is Bud23 needed for A1 cleavage in addition to A2 processing? Processing of the rRNA is initiated cotranscriptionally on the primary 35S transcript by cleavage at site A0. Subsequent cleavages at A1 and A2 liberate the 20S rRNA intermediate found in the pre-40S particle that is exported to the cytoplasm. Current structures of the SSU Processome contain RNA cleaved at A0, but not A1 (Barandun et al., 2017; Cheng et al., 2017) consistent with our understanding that A0 cleavage is prior to A1. In these structures, the A2 site within ITS1 is not resolved, but Northern blotting suggests that it is not cleaved (Chaker-Margot et al., 2017; Sun et al., 2017). How cleavage at A1 and A2 are regulated is not understood but it has been postulated that conformational changes driven by Bms1 reposition the endonucleolytic PIN domain of Utp24 for cleavage at A1 (Cheng et al., 2017).

We previously showed that in the absence of Bud23, A2 cleavage is inhibited (White et al., 2008). Consistent with this conclusion, we found that 21S RNA (cleaved at A1 and A3 but not A2) accumulated in whole cell extracts of *bud23*Δ mutants (Figs. 2E & 4B) and in pre-40S particles affinity purified with Enp1 when Bud23 was depleted (Fig. 7B). We were surprised that in addition to 21S RNA, we observed approximately equivalent amounts of 22S RNA in these particles. 22S RNA arises when cleavages at both A1 and A2 are blocked. This result suggests that, in the absence of Bud23, processing at A1 is slowed while A2 processing is strongly inhibited. Moreover, this result links Bud23 to A1 cleavage and suggests that Bud23 acts at an earlier step in pre-40S assembly than previously thought. Intriguingly, we found that mutations in Bms1 suppress the absence of Bud23 suggesting that Bud23 could impinge on A1 cleavage through Bms1. The C-terminal domain of Bms1 is thought to remodel RNA to allow Utp24 to access the A1 site (Cheng et al., 2017). The C-terminal domain connects to domain IV of Bms1 through an unstructured

bioRxiv preprint doi: https://doi.org/10.1101/2020.02.05.936237; this version posted February 6, 2020. The copyright holder for this preprint (which was not certified by peer review) is the author/funder. All rights reserved. No reuse allowed without permission.

strand that lays over domain III, and it is in this interface that we find most of the *bud23*Δ-suppressing mutations. Bms1 is structurally related to EF-Tu (Fig. S4A), which delivers aminoacylated tRNAs to the ribosome (reviewed in (Maracci and Rodnina, 2016)). Activation of EF-Tu GTPase activity induces conformational changes that release the tRNA. Intriguingly, in the SSU Processome structure, it is the C-terminal connector strand of Bms1 as well as a helix of Mpp10 that occupy the volume corresponding to tRNA in EF-Tu (Figs. S4E & S4F). Thus, the GTPase activity of Bms1 could induce a conformational change to release the C-terminal connector, repositioning Utp24 for A1 cleavage. Because mutations in Bms1 that are poised to release the C-terminal connector bypass the absence of Bud23, Bud23 recruitment to the SSU Processome could trigger Bms1 conformational changes. Intriguingly, *bud23*Δ also shows strong negative genetic interaction with a hypomorphic *utp24* allele (Sardana et al., 2013). In this work we have used a genetic approach to develop a conceptual framework for understanding the progression of the SSU Processome into the pre-40S particle. Biochemical and structural analysis are now needed to test the ideas that we have presented here.

Materials and methods

Strains, growth media, genetic methods, and yeast two-hybrid (Y2H) analysis. All S. cerevisiae strains and sources are listed in Table 1. AJY2676 was generated by genomic integration of *Eco*RI-digested pAJ4339 (Tong et al., 2001) into AJY2161 to replace the *KanMX* marker with *CloNAT*. AJY3156 was generated by genomic integration of *bud23*Δ*::KanMX* into AJY2665. AJY4175 was generated by transforming pAJ4094 into a *UTP2/utp2*Δ*::KanMX* heterozygous diploid strain (Winzeler et al., 1999), sporulated, and dissected. AJY4395 was generated by genomic integration

bioRxiv preprint doi: https://doi.org/10.1101/2020.02.05.936237; this version posted February 6, 2020. The copyright holder for this preprint (which was not certified by peer review) is the author/funder. All rights reserved. No reuse allowed without permission.

634 of *AID-HA::OsTIR1::LEU2* amplified from pJW1662 (Costa et al., 2018) into the *BUD23* locus of
635 AJY2665. All yeast strains were cultured at 30°C in either YPD (2% peptone, 1% yeast extract, 2%
636 dextrose), YPgal (2% peptone, 1% yeast extract, 1% galactose), or synthetic dropout (SD) medium
637 containing 2% dextrose unless otherwise noted. When appropriate, media were supplemented
638 with 150 to 250 µg/ml G418 or 100 µg/ml nourseothricin. All plasmids and sources are listed in
639 Table 2. Y2H analysis was performed as previously described (Black et al., 2018).
640
641 **Identification of additional spontaneous suppressors of *bud23*Δ.** AJY2676 cells were inoculated
642 into 200 µL of YPD media in a 48-well format plate. Cells were cultured with continuous shaking
643 until saturation then diluted into fresh media. After each passage, cells were plated onto YPD
644 plates to test for the presence of suppressors. This process was iterated for each culture until
645 suppressors were observed. Single colonies of each suppressor strain were obtained and genomic
646 DNA was prepped using MasturePure™ Yeast DNA Purification Kit (Lucigen). The *DHR1*, *IMP4*,
647 *UTP2*, and *UTP14* loci were amplified and sequenced by Sanger to identify mutations in known
648 suppressors (Sardana, 2013; Sardana et al., 2014, 2013; Zhu et al., 2016).
649 Libraries for the six strains that did not carry suppressors in *DHR1*, *IMP4*, *UTP2* or *UTP14*
650 were prepared and sequenced on an Illumina NextSeq 500 platform by the Genomic Sequencing
651 and Analysis Facility at the University of Texas at Austin. The quality of the resultant reads was
652 assessed using FastQC (v0.10.1) [http://www.bioinformatics.babraham.ac.uk/projects/fastqc/],
653 and subsequently processed using TrimGalore (v1.14)
654 [http://www.bioinformatics.babraham.ac.uk/projects/trim_galore/] to discard low-quality
655 sequences and adapters. The processed reads were aligned using Bowtie2 (v2.3.4) (Langmead

bioRxiv preprint doi: https://doi.org/10.1101/2020.02.05.936237; this version posted February 6, 2020. The copyright holder for this preprint (which was not certified by peer review) is the author/funder. All rights reserved. No reuse allowed without permission.

and Salzberg, 2012) using the default settings for paired-end reads. The resultant files were further processed with SAMtools (v0.1.18) (Li et al., 2009) and BCFtools (v0.1.17) (Narasimhan et al., 2016) to generate variant call format files. VCFtools (v0.1.16) (Danecek et al., 2011) was used to filter out variants with low quality scores (Quality value < 100) and to compare samples pairwise to identify mutations unique to each suppressed strain. This analysis revealed single point mutations within *BMS1* and *RPS28A* that were confirmed by Sanger sequencing. The *bms1* and *rps28a* variants were subsequently cloned into centromeric vectors and, as with all other *bud23*Δ suppressors that we have identified, the *rps28A* and *bms1* mutants were dominant (data not shown). All mutant strains isolated in this screen are listed in Table 1.

Identification of mutations in *UTP2* that suppress *bud23*Δ. Random mutations in *UTP2* were generated by error-prone PCR using *Taq* polymerase and pAJ2595 as the template and oligos that hybridize to the upstream and downstream sequences of *UTP2*. The restriction enzymes *Eco*RI and *Sph*I were used to linearize the vector pAJ2595 and the linearized vector was, co-transformed with the mutant amplicon into AJY2161, and plated onto SD-Uracil media to allow recombination of the mutant amplicon into the pAJ2595 backbone. Colonies displaying a suppressed phenotype were isolated; vectors were rescued from yeast and sequenced after confirming that the vectors conferred suppression.

Affinity purification. Cells were cultured as described in the Northern blotting and mass spectrometry subsections below. All steps were carried out on ice or at 4°C. Cells were washed with Lysis Buffer (50 mM Tris-HCl pH 7.6 (25°C), 100 mM KCl, 5 mM $MgCl_2$, 5 mM beta-

bioRxiv preprint doi: https://doi.org/10.1101/2020.02.05.936237; this version posted February 6, 2020. The copyright holder for this preprint (which was not certified by peer review) is the author/funder. All rights reserved. No reuse allowed without permission.

678 mercaptoethanol (βME), 1 mM each of PMSF and Benzamidine, and 1 µM each of leupeptin and
679 pepstatin) supplemented with EDTA-free Pierce Protease Inhibitor Mini Tablet cocktail (Thermo
680 Scientific), then resuspended in 1 volume Lysis Buffer. Extracts were generated by glass bead lysis
681 and clarified at 18,000*g* for 15 minutes. Clarified extracts were normalized according to A_{260} and
682 supplemented with 0.1% TritonX-100. Normalized extracts were incubated for 1.5 hours with
683 rabbit IgG (Sigma) coupled to Dynabeads (Invitrogen), prepared as previously described
684 (Oeffinger et al., 2007). Following binding, the beads were washed thrice with Wash Buffer (Lysis
685 Buffer supplemented with 0.1% TritonX-100). The beads were resuspended in Elution Buffer
686 (Wash Buffer supplemented with TEV protease and Murine RNase Inhibitor (New England
687 Biolabs)) and the bound Enp1-TAP containing complexes were eluted for 1.5 – 2 hours. The
688 resultant eluates were handled as described in the Northern blotting and mass spectrometry
689 subsections below.
690
691 **Northern blot analysis.** For analysis of rRNA processing in whole cell extract (WCE), strains were
692 cultured overnight in YPD media to saturation. Cell cultures were diluted into YPD at a starting
693 OD_{600} of 0.1 and cultured to mid-exponential phase (OD_{600} ~0.4-0.5) before collection and storage
694 at -80°C prior to lysis. For analysis of affinity purified RNAs, strains AJY2665 and AJY4395 were
695 cultured overnight in YPD media to saturation. Cells were diluted into YPD at a starting OD_{600} of
696 0.05 and cultured for three hours. Cultures were treated with 0.5 mM auxin for 2 hours at 30°C,
697 centrifuged, and frozen in liquid nitrogen. Affinity purification was performed as described above.
698 Affinity purified and WCE RNAs were isolated using the acid-phenol-chloroform method as
699 previously described (Zhu et al. 2016). RNAs were electrophoresed through 1.2%-agarose MOPS

bioRxiv preprint doi: https://doi.org/10.1101/2020.02.05.936237; this version posted February 6, 2020. The copyright holder for this preprint (which was not certified by peer review) is the author/funder. All rights reserved. No reuse allowed without permission.

6% formaldehyde gel. Northern blotting was performed as previously described (Li et al. 2009) using the oligo probes listed in the legends of Figures 2 and 7, and signal was detected by phosphoimaging on a GE Typhoon FLA9500.

Mass spectrometry and analysis. Strains AJY2665 and AJY4395 were cultured as described in the Northern blot analysis subsection. Affinity purifications were performed as described above. To isolate factors associated with only preribosomal particles, the eluate was overlaid onto a sucrose cushion (15% D-sucrose, 50 mM Tris-HCl pH 7.6 (25°C), 100 mM KCl, 5 $MgCl_2$) then centrifuged at 70,000 rpm for 15 min in a Beckman Coulter TLA100 rotor. Following, the pellets were precipitated with 15% trichloroacetic acid (TCA), washed with acetone and dried, and resuspended in 1X Laemmli buffer. Approximately equivalent amounts of protein were either fully separated on SDS-PAGE gels for excision of individual species or electrophoresed slightly into a NuPAGE Novex 4%–12% Bis-Tris gel for analysis of the entire affinity purification. Peptides were recovered from in-gel Trypsin digestion and prepared for identification by mass spectrometry as previously described (Black et al., 2018). The resultant peptides were identified at The University of Texas at Austin Proteomics Facility by LC-MS/MS on a Thermo Orbitrap Fusion 1 with either a 30 minute or 1 hour run time for identification of single species or complex sample, respectively. Mass spectrometry data were processed in Scaffold v4.8.3 (Proteome Software, Inc.). A protein threshold of 99% minimum with two peptides minimum and peptide threshold of 1% false discovery rate was applied. The data were exported, and custom Python 2.7 scripts were used to calculate the relative spectral abundance factor (RSAF) for each protein by dividing the total number of spectral counts by the molecular weight. Values for each protein

bioRxiv preprint doi: https://doi.org/10.1101/2020.02.05.936237; this version posted February 6, 2020. The copyright holder for this preprint (which was not certified by peer review) is the author/funder. All rights reserved. No reuse allowed without permission.

were normalized to the bait, Enp1, to reflect relative stoichiometry. Supplemental File 1 contains relevant spectral counts and processed data from the mass spectrometry experiments.

Sucrose density gradient analysis. For polysome profile analysis of the suppressors of *bud23*Δ, BY4741, AJY2676, AJY3744, AJY4529, AJY4531, and AJY4535 were cultured overnight in YPD to saturation. Cultures were diluted into YPD at a starting OD_{600} of 0.02 and cultured to early exponential phase (OD_{600}~0.10-0.13) and then treated with cycloheximide (CHX) at 100 µg/ml for 10 minutes at 30°C to inhibit translation. After centrifugation cells were frozen in liquid nitrogen and stored at -80°C. Cells were washed and resuspended in Lysis Buffer (50 mM Tris-HCl pH 7.6 (25°C), 100 mM KCl, 5 mM $MgCl_2$, 7 mM βME, 100 µg/mL CHX, 1 mM each of PMSF and Benzamidine, and 1 µM each of leupeptin and pepstatin). Extracts were prepared by glass bead lysis and clarified by centrifugation for 15 minutes at 18,000*g* at 4°C. 4.5 A_{260} units of clarified extract were loaded onto 7-47% sucrose gradients made in the same buffer lacking protease inhibitors. Gradients were subjected to ultracentrifugation for 2.5 hours at 40,000 rpm in a Beckman SW40 rotor. The gradients were subjected to continuous monitoring at 254 nm using an ISCO Model 640 fractionator.

For analysis of the sedimentation of factors in the absence of Bud23, AJY2665 and AJY4395 were cultured overnight to saturation. Cells were diluted into YPD at a starting OD_{600} of 0.05 and cultured for three hours (OD_{600} =~0.08-0.1). Cultures were treated with 0.5 mM auxin for 2 hours at 30°C, then treated with CHX at 100 µg/mL for 10 minutes at 30°C. Cells were harvested and stored as described above. Cells were washed and resuspended in Lysis Buffer supplemented with an EDTA-free Pierce Protease Inhibitor Mini Tablet cocktail (Thermo

bioRxiv preprint doi: https://doi.org/10.1101/2020.02.05.936237; this version posted February 6, 2020. The copyright holder for this preprint (which was not certified by peer review) is the author/funder. All rights reserved. No reuse allowed without permission.

744 Scientific). Extracts were generated, and nine A_{260} units were loaded onto sucrose gradients and
745 subject to ultracentrifugation as described above. Gradients were fractionated into 600 µL
746 fractions with continuous monitoring at 254 nm using an ISCO Model 640 fractionator. Each
747 fraction was split in half to collect proteins and RNAs. Proteins were precipitated using 15% TCA
748 as described previously (Black et al., 2018). One-fifth of protein from each half fraction was
749 separated on SDS-PAGE gels and subjected to Western blotting. RNAs were precipitated as
750 described previously (Musalgaonkar et al., 2019) supplemented with 10 µg of glycogen. One-third
751 of RNA from each half fraction was subjected to Northern blotting as described above.
752
753 **Western blot analysis.** Primary antibodies used in this study were anti-c-Myc monoclonal 9e10
754 (Biolegend), anti-HA (Biolegend), anti-Bud23 (C. Wang), anti-Rps24 (our laboratory), anti-
755 Glucose-6-phosphate dehydrogenase (Sigma ImmunoChemicals), and anti-Imp4 (S. Baserga).
756 Secondary anti-bodies were goat anti-mouse antibody-IRDye 800CW (Li-Cor Biosciences), goat
757 anti-rabbit antibody-IRDye 680RD (Li-Cor Biosciences), and goat anti-rabbit antibody-HRP
758 (Jackson Immunoresearch Laboratories). The blots in Figs. 3D, 3F, 5C, and 6B were imaged with
759 an Odyssey CLx infrared imaging system (Li-Cor Biosciences) using Image Studio (Li-Cor
760 Biosciences). The blots in Fig. 6C were imaged using SuperSignal West Pico PLUS
761 Chemiluminescent Substrate (Thermo Scientific) and exposed to film.
762
763 **Molecular visualization.** All images of SSU Processome and Dhr1 structures are from PDB
764 ascension codes 5WLC and 6H57, respectively. The structures of GDPNP- and GDP-bound EF-Tu

bioRxiv preprint doi: https://doi.org/10.1101/2020.02.05.936237; this version posted February 6, 2020. The copyright holder for this preprint (which was not certified by peer review) is the author/funder. All rights reserved. No reuse allowed without permission.

765 are from PDB ascension codes 1B23 and 1EFC, respectively. Molecular visualizations were
766 generated using MacPyMOL: PyMOL v1.8.2.1 Enhanced for Mac OS X (Schrödinger LLC).
767

768 ## Figure legends

769 **Figure 1. Extragenic suppressors of *bud23*Δ reveal an interaction network that connects the 3'**
770 **basal subdomain to the U3-18S heteroduplexes.** (A) A secondary structure map of the 18S rRNA
771 that indicates the position of the 3' basal subdomain (dark gray) and the central pseudoknot (CPK;
772 deep olive). (B) The position of the 3' basal subdomain (dark gray) within the context of the SSU
773 Processome structure (light gray). (C) Factors harboring mutations that suppress *bud23*Δ and are
774 resolved in the SSU Processome (PDB 5WLC) cluster around the 3' basal subdomain and the U3-
775 Box A'-18S heteroduplex that Dhr1 unwinds. Shown are: Bms1 (forest green), Imp4 (blue), Rps28
776 (cyan), Utp2 (orange), Utp14 (brown), U3 (deep purple), 18S rRNA (deep olive), 3' basal
777 subdomain (dark gray). (D) Zoomed view of factors in C showing contacts amongst each other,
778 the 3' basal subdomain, and the U3-Box A'-18S heteroduplex. N- and C-terminal domains, NTD
779 and CTD, respectively. The U3-18S heteroduplexes are shown as U3 Box A and U3 Box A'.
780 Guanosine 1575 (G1575, red) is shown as a marker for the binding site of Bud23. (E) Tabulation
781 of the number of unique mutations found in each extragenic suppressor of *bud23*Δ. Newly
782 identified mutations (novel) and previously identified (known) (Sardana, 2013; Sardana et al.,
783 2014, 2013; Zhu et al., 2016). (F) Summary of the genetic and physical interactions amongst the
784 suppressors of *bud23*Δ. Factors are indicated as nodes; genetic and physical interactions are
785 shown as dashed and solid edges, respectively.
786

bioRxiv preprint doi: https://doi.org/10.1101/2020.02.05.936237; this version posted February 6, 2020. The copyright holder for this preprint (which was not certified by peer review) is the author/funder. All rights reserved. No reuse allowed without permission.

Figure 2. The Imp4 and Rps28A mutations primarily map to their interfaces with the 3' basal subdomain. (A) Point mutations within *imp4* and *rps28a* suppressed the growth defect of *bud23*Δ as shown by 10-fold serial dilutions of wild-type cells (BY4741), *bud23*Δ (AJY2676), and *bud23*Δ-suppressed cells spotted on YPD media and grown for two days at 30°C. (B) Rps28 and the Brix domain of Imp4 interact with the 3' basal subdomain RNA, while the NTD of Imp4 makes contacts with its Brix domain and the U3-18S heteroduplexes. G1575, the binding site of Bud23, is shown for reference. The regions where the mutated residues map are indicated by magenta and green dashed boxes for the rRNA interaction and the NTD interaction, respectively. Factors are colored the same as in Fig. 1. (C) Residues mutated in Rps28 and Imp4 Brix domain map to interaction interfaces with the 3' basal subdomain RNA (magenta sticks). (D) Several residues mutated in Imp4 map to an intramolecular interaction between the Brix and NTD of Imp4 (green sticks). (E) Suppressing mutations in *imp4* and *rps28a* partially restored A2 processing and 18S rRNA levels in *bud23*Δ cells. RNA processing intermediates were detected by Northern blotting on RNAs extracted from wild-type (WT), *bud23*Δ, and *bud23*Δ-suppressed cells cultured to exponential phase at 30°C in liquid YPD. P32-radiolabeled probes (Table 3) hybridized to the indicated regions. The 25S and 18S rRNAs were detected by methylene blue staining of the RNAs prior to oligo hybridization. (F) The *imp4* and *rps28a* mutations partially restored 40S biogenesis as shown by polysome profiles after separation of extracts on sucrose density gradients from wild-type, *bud23*Δ, and *bud23*Δ-suppressed cells cultured to exponential phase at 30°C in liquid YPD media.

Figure 3. The mutations in Utp2 disrupted its interaction with Imp4. (A) Spontaneous point mutations within *utp2* partially suppressed the growth defect of *bud23*Δ as shown by 10-fold

bioRxiv preprint doi: https://doi.org/10.1101/2020.02.05.936237; this version posted February 6, 2020. The copyright holder for this preprint (which was not certified by peer review) is the author/funder. All rights reserved. No reuse allowed without permission.

809 serial dilutions of wild-type cells (BY4741), *bud23*Δ (AJY2676), and *bud23*Δ-suppressed cells
810 spotted on YPD media and grown for two days at 30°C. (B) Additional point mutations in *UTP2,*
811 generated by error-prone PCR, also suppressed the growth defect of *bud23*Δ (left) and
812 complemented loss of *UTP2* (right) as shown by 10-fold serial dilutions of *bud23*Δ (AJY2676) and
813 *PGAL10-UTP2* (AJY4175) cells containing either empty vector, or vectors encoding the indicated
814 alleles of *UTP2* spotted on SD-Leu media containing glucose and grown for two days at 30°C. (C)
815 Several of the mutations in Utp2 map to residues (green sticks) located within its NTD (orange)
816 that interacts with the Brix domain of Imp4 (blue) adjacent to the 3' basal subdomain RNA (gray).
817 (D) Left: Yeast two-hybrid interaction assay between Imp4 and wild-type (WT) or mutant Utp2.
818 Strains carrying the indicated constructs were patched onto Leu- Trp- (L-W-) and Leu-Trip-His- (L-
819 W-H-) media supplemented with 2 mM 3-Amino-1,2,4-triazole (3AT) (AD, Gal4 activation domain;
820 BD, Gal4 DNA binding domain). Right: Western blot analysis of the wild-type and mutant Utp2-
821 AD-HA proteins using equivalent amounts of total protein extracts. Glucose-6-phosphate
822 dehydrogenase (G6PDH) was used as a loading control. (E) Top: F58 of Utp2 (green sticks) fits
823 into a hydrophobic pocket in the Brix domain of Imp4 (surface representation). Bottom: The
824 *bud23*Δ-suppressing mutations V170F and P252L of Imp4 (magenta sticks) line this pocket. Imp4
825 and Utp2 are colored blue and orange, respectively. (F) Top: Yeast two-hybrid interaction assay
826 between Utp2 and wild-type or mutant Imp4. Strains carrying the indicated constructs were
827 patched onto L-W- and L-W-H- media supplemented with 6 mM 3AT. Bottom: Western blot
828 analysis of the wild-type and mutant BD-myc-Imp4 proteins in equivalent amounts of total
829 protein extract is shown. G6PDH was used as a loading control.
830

bioRxiv preprint doi: https://doi.org/10.1101/2020.02.05.936237; this version posted February 6, 2020. The copyright holder for this preprint (which was not certified by peer review) is the author/funder. All rights reserved. No reuse allowed without permission.

Figure 4. The mutations in the GTPase Bms1 that suppress *bud23*Δ are poised to modulate its conformational state. (A) Spontaneous point mutations within *BMS1* suppressed the growth defect of *bud23*Δ as shown by 10-fold serial dilutions of wild-type cells (BY4741), *bud23*Δ (AJY2676), and *bud23*Δ cells carrying the indicated *bms1* mutations spotted on YPD media and grown for two days at 30°C. (B) The *bms1* mutations partially restored A2 processing and 18S rRNA production in *bud23*Δ cells as shown by Northern blotting of RNAs extracted from wild-type, *bud23*Δ, and *bud23*Δ-suppressed cells as described in Fig. 2E. (C) The *bms1* mutations partially restored 40S biogenesis as shown by the analysis of the polysome profiles from the indicated strains as described in Fig. 2F. (D) Top: Primary structure of Bms1 with domains (in different shades of green), interacting regions and *bud23*Δ suppressing mutations annotated; regions not resolved in SSU Processome structures are indicated in light gray. Bottom: The partial structure of Bms1 (from PDB 5WLC) in the context of the SSU Processome is shown. Domains IV and V extend from its GTPase core (domains I – III) to contact the RNAs of the 3' basal subdomain (gray) and the U3-18S heteroduplexes (pink/gold), respectively. (E) At the 3' basal subdomain, Domain IV of Bms1 also contacts the CTDs of Utp2 (orange) and Imp4 (blue). (F) The mutated residues D124, D843, A903, and S1020 in Bms1 map to inter-domain contacts with the unstructured strand of domain V that connects it to domain IV.

Figure 5. Most of the Dhr1 mutations map to surface residues of its RecA domains. (A) A cartoon of the primary structure of Dhr1 is shown. The domains of Dhr1 are annotated by color: NTD, N-terminal domain (light gray); RecA1/2, Recombination protein A1/2 (blue/green); WH, winged-helix (yellow); HB, helical bundle (orange); OB, oligonucleotide-binding fold (brown); CTD, C-

bioRxiv preprint doi: https://doi.org/10.1101/2020.02.05.936237; this version posted February 6, 2020. The copyright holder for this preprint (which was not certified by peer review) is the author/funder. All rights reserved. No reuse allowed without permission.

terminal domain (light red). Unstructured regions are colored as light gray. Mutations reported here (novel) and previously (known) (Sardana et al., 2014) are indicated as black and magenta, respectively. Numbering indicates residue numbering of yeast Dhr1. (B) The structure of yeast Dhr1 (PDB 6H57) with relevant features colored as described in panel A. Catalytic residues involved in ATP hydrolysis are denoted as red sticks for reference. (C) The majority of the mutated residues map to the surfaces of the RecA domains. Mutated residues are shown as black and magenta sticks as described for panel A. The positions of the residues that were used to test loss-of-interaction with Utp14 in panel D are indicated. (D) Top: Yeast two-hybrid interaction data between AD-HA-Utp14 and wild-type (WT) or mutant BD-myc-Dhr1 are shown. Strains carrying the indicated constructs were patched onto Leu- Trp- (L-W-) and Leu-Trip-His- (L-W-H-) media supplemented with 10 mM 3-Amino-1,2,4-triazole (3AT) (AD-HA, GAL4AD-HA; BD-myc, GAL4BD-myc). Bottom: Western blot analysis of the wild-type and mutant BD-myc-Dhr1 proteins using equivalent amounts of total protein extracts is shown. Glucose-6-phosphate dehydrogenase (G6PDH) was used as a loading control.

Figure 6. Imp4 and Enp1 accumulate with pre-40S upon Bud23 depletion. (A) The genomic fusion of an auxin-inducible degron (AID) to the C-terminus of Bud23 rendered cells sensitive to auxin, with a growth defect comparable to *bud23*Δ. 10-fold serial dilutions of wild-type (AJY2665), *BUD23-AID* (AJY4395), and *bud23*Δ (AJY3156) cells were spotted on YPD media with and without 0.5 mM auxin and grown for two days at 30°C. (B) Western blot of time-course of depletion of Bud23-AID, using equivalent amounts of total protein extract from AJY2665 or AJY4395 cells cultured to exponential phase then harvested prior to or after the addition of 0.5

bioRxiv preprint doi: https://doi.org/10.1101/2020.02.05.936237; this version posted February 6, 2020. The copyright holder for this preprint (which was not certified by peer review) is the author/funder. All rights reserved. No reuse allowed without permission.

875 mM auxin for the indicated time (WT; wild-type). G6PDH was used as a loading control. (C) The
876 sucrose density gradient sedimentation of SSU Processome factors in the presence (left panel) or
877 absence (right panel) of Bud23. Extracts were prepared from + Bud23 (AJY2665) and - Bud23
878 (AJY4395) cells treated with 0.5 mM auxin for two hours prior. Western blots were done for Enp1,
879 Imp4 and Rps24. U3 snoRNA was detected by Northern blotting with a complementary P32-
880 radiolabeled probe. 25S and 18S were visualized with methylene blue stain. Oligo probes are
881 listed in Table 3.
882
883 **Figure 7. Composition of 40S precursors purified in the absence of Bud23.** (A) Coomassie-
884 stained gel of proteins that co-purified with Enp1-TAP in the presence (+) or absence (-) of Bud23.
885 Pre-ribosomal particles were enriched by overlaying eluate onto sucrose cushions followed by
886 ultracentrifugation. Individual species that showed clear enrichment or depletion were excised
887 and identified by mass spectrometry and are indicated in blue or black text, respectively. The
888 asterisks (*) denote proteins that also appeared in the analysis described in Fig. S6. (B) The rRNA
889 processing intermediates and U3 snoRNA that co-purified with Enp1-TAP in the presence (+) or
890 absence (-) of Bud23 were detected by Northern blotting using the indicated probes. Oligos are
891 listed in Table 3.
892
893 **Figure 8. Models for Bud23 function in SSU Processome progression.** (A) A cartoon 2-
894 dimensional projection of Fig. 1D showing factors surrounding the 3' basal subdomain (gray) and
895 U3-18S heteroduplexes (magenta/gold). During assembly of the SSU Processome, multiple
896 contacts are formed amongst Bms1 (green), Imp4 (blue), and Utp2 (orange). These three proteins

bioRxiv preprint doi: https://doi.org/10.1101/2020.02.05.936237; this version posted February 6, 2020. The copyright holder for this preprint (which was not certified by peer review) is the author/funder. All rights reserved. No reuse allowed without permission.

contain long helical extensions that support the U3-18S heteroduplexes but block their access by Dhr1 (light blue). Bms1, Imp4, and Utp2 all have extensive interactions with the 3' basal subdomain rRNA that connect events here to the U3-18S heteroduplexes. In this state, U3 is inaccessible by Dhr1. Two possible mechanisms can occur here. (B) After final SSU Processome compaction, Bud23 (yellow) binds to the 3' basal subdomain and signals to Bms1 to activate its GTPase domain. This, in turn, leads to conformational changes that displace the helical extensions of these proteins away from the U3-18S heteroduplexes allowing Dhr1 to gain access so that it can unwind it to initiate SSU Processome progression. (C) Alternatively, Dhr1 may first translocate through the U3 Box A-18S heteroduplex until it is stopped by the helical extensions. In this model, Bud23 binding to the 3' basal subdomain signals to Bms1 as in panel B. Bms1 activity drives conformational changes to allow Dhr1 to continue its translocation through the U3 Box A'-18S heteroduplex allowing subsequent SSU Processome progression to occur.

Supplemental figure legends

Figure S1. Schematic of rRNA processing relevant to 40S production in *S. cerevisiae*. Processing of the pre-18S rRNA at sites A0, A1, and A2 (or A3) occurs within the context of the SSU Processome. Cleavage at either the A2 or A3 sites liberates the SSU precursors from the LSU precursors containing the 27SA2 and 27SA3 rRNA intermediates, respectively. Processing of A0, A1, and A2 (or A3) appear to occur in a sequential order to produce the 20S rRNA intermediate. The 20S rRNA is a component of the pre-40S particles that are exported to the cytoplasm where a final cleavage event at the D site yields the 18S rRNA.

bioRxiv preprint doi: https://doi.org/10.1101/2020.02.05.936237; this version posted February 6, 2020. The copyright holder for this preprint (which was not certified by peer review) is the author/funder. All rights reserved. No reuse allowed without permission.

919 **Figure S2. Secondary structure diagram of the 18S rRNA.** The 18S rRNA is divided into four main
920 domains: the 5' domain (blue), Central domain (gold), 3' Major domain (purple and black), and
921 the 3' Minor domain (green). The 3' basal subdomain (black) is a sub-region of the 3' Major
922 domain that forms during the assembly of the SSU Processome (Sun et al., 2017), and contains
923 the binding site for Bud23. The base methylated by Bud23, guanosine 1575 (G1575, red) is
924 indicated. The position of the Central Pseudoknot (CPK, gray) is also pictured.
925
926 **Figure S3. The position of Utp14 and the binding site of Dhr1 within the SSU Processome.** (A)
927 The location of the resolved segments of Utp14 (brown) in the SSU Processome. A contour line
928 indicates the unresolved region of Utp14 where the Dhr1-interaction surface and *bud23*Δ-
929 suppressing mutations are located. The U3 snoRNA binding site of Dhr1 and U3 mutations that
930 suppress a cold-sensitive Dhr1 mutant (Sardana et al., 2015) are indicated by cyan and black
931 sticks, respectively. Bms1, Imp4, Rps28, Utp2, and the 3' basal subdomain RNA are shown for
932 reference. (B) A cartoon of Utp14 primary structure indicating the position of its resolved
933 portions and the *bud23*Δ-suppressing mutations reported here (black) and previously (light blue)
934 within its Dhr1-activaction loop (Zhu et al., 2016).
935
936 **Figure S4. Comparison of the structure of Bms1 to the conformational states of EF-Tu.** (A)
937 Structural alignment of EF-Tu bound to the non-hydrolysable GTP analog, GDPNP (slate blue, PDB
938 1B23) to domain I of Bms1 (from PDB 5WLC) is shown. Bms1 is colored by domains as in Fig. 4D;
939 the GTP analog and magnesium ion bound to EF-Tu are shown as orange sticks and green sphere.
940 Structures are shown individually (left, middle) and as an overlay (right). (B) A view of domains II

bioRxiv preprint doi: https://doi.org/10.1101/2020.02.05.936237; this version posted February 6, 2020. The copyright holder for this preprint (which was not certified by peer review) is the author/funder. All rights reserved. No reuse allowed without permission.

941 and III of Bms1 compared to those of EF-Tu shows that the two domains adopt beta barrels in
942 similar conformations. (C) GDPNP-bound EF-Tu forms a complex with tRNA, while GDP-bound EF-
943 Tu (deep purple, PDB 1EFC) does not. (D) Conformational differences in the beta-barrel domains
944 of GDP and GTP-bound EF-Tu suggest that these domains rotate away from one another upon
945 GTP hydrolysis to promote tRNA release. (E) The amino-acyl tRNA contacts GDPNP-bound EF-Tu
946 through its two beta barrel domains. (F) Bms1 in the same orientation as EF-Tu in panel E. The
947 unstructured loop of domain V that connects it to domain IV (denoted by the black arrow) and
948 an N-terminal helix of Mpp10 (red) contacts domains II and III of Bms1 in a manner reminiscent
949 of how tRNA interacts with GDPNP-bound EF-Tu. The mutated residues that suppress *bud23*Δ are
950 shown as magenta sticks.
951
952 **Figure S5. Proteomic compositions of 40S pre-cursors from cells with or without Bud23.** Related
953 to Figure 7. A heatmap of SSU biogenesis proteins that co-immunoprecipitated with Enp1-TAP in
954 the presence (+) or absence (-) of Bud23 is shown. The scale spanning from 0 (white) to 1 (cyan)
955 reflects the relative spectral abundance factor (RSAF). The RSAF was calculated by first
956 normalizing the total number of spectral counts identified for a given protein to its molecular
957 weight; these values were further normalized to the bait, Enp1, to reflect stoichiometry. RSAF
958 values for each protein are shown within each cell. For each protein, the number of spectral
959 counts identified in the presence or absence of Bud23 are shown in parentheses, respectively.
960 Proteins that showed a significant increase or decrease relative to the + Bud23 sample and are
961 listed in Fig. S6 are denoted by an asterisks (*) colored blue or black, respectively. Proteins are
962 grouped according to (Zhang et al., 2016) or by known function. Heatmaps were generated in

bioRxiv preprint doi: https://doi.org/10.1101/2020.02.05.936237; this version posted February 6, 2020. The copyright holder for this preprint (which was not certified by peer review) is the author/funder. All rights reserved. No reuse allowed without permission.

963 Graphpad Prism version 8.3.0 (328) for Mac iOS. The complete data for this figure are available
964 in Supplemental File 1.
965
966 **Figure S6. 40S biogenesis factors whose association with 40S pre-cursors significantly changed**
967 **upon Bud23-depletion.** Related to Figures 7 and S5. Mass spectrometry analysis of total proteins
968 that co-precipitated with Enp1. Proteins that showed a significant log2 fold-change difference in
969 the absence or presence or Bud23 are shown. Total number of peptides identified for each
970 protein was normalized to molecular weight then further normalized to the bait to generate RSAF
971 values (see Methods) which were used to calculate the log2 fold-change between the mutant
972 and wild-type samples. Proteins displaying a ± 0.5-fold change or more with a difference of
973 greater than 10 total spectral counts are plotted. Proteins are grouped according to when they
974 first bind to pre-ribosomes (Zhang et al., 2016). The complete mass spectrometry data are
975 available in Supplemental File 1.
976

977 ## Tables

978 **Table 1: Yeast strains used in this study.**

Strain	Genotype	Reference
AJY2665	*MATa his3Δ1 leu2Δ0 met15Δ0ura3Δ0 ENP1-TAP::HIS3MX6*	(Ghaemmaghami et al., 2003)
AJY2161	*MATa his3Δ1 leu2Δ0 ura3Δ0 lys2Δ0 met15Δ0 bud23Δ::KanMX*	(White et al., 2008)
AJY2676	*MATa his3Δ1 leu2Δ0 ura3Δ0 lys2Δ0 met15Δ0 bud23Δ::CloNAT*	This study & (Sardana, 2013).
AJY3156	*MATa his3Δ1 leu2Δ0 met15Δ0ura3Δ0 ENP1-TAP::HIS3MX6 bud23Δ::KanMX*	This study.
AJY3581	*MATa his3Δ1 leu2Δ0 ura3Δ0 lys2Δ0 met15Δ0 bud23Δ::KanMX*	(Sardana et al.,

bioRxiv preprint doi: https://doi.org/10.1101/2020.02.05.936237; this version posted February 6, 2020. The copyright holder for this preprint (which was not certified by peer review) is the author/funder. All rights reserved. No reuse allowed without permission.

	utp2-A2D	2013)
AJY3512	*MATa his3Δ1 leu2Δ0 ura3Δ0 lys2Δ0 met15Δ0 bud23Δ::KanMX imp4-V170F*	This study & (Sardana, 2013).
AJY3579	*MATa his3Δ1 leu2Δ0 ura3Δ0 lys2Δ0 met15Δ0 bud23Δ::KanMX imp4-R94L*	This study & (Sardana, 2013).
AJY3580	*MATa his3Δ1 leu2Δ0 ura3Δ0 lys2Δ0 met15Δ0 bud23Δ::KanMX imp4-N118K*	This study & (Sardana, 2013).
AJY3741	*MATa his3Δ1 leu2Δ0 ura3Δ0 lys2Δ0 met15Δ0 bud23Δ::KanMX imp4-T92I*	This study & (Sardana, 2013).
AJY3742	*MATa his3Δ1 leu2Δ0 ura3Δ0 lys2Δ0 met15Δ0 bud23Δ::KanMX imp4-R116M*	This study & (Sardana, 2013).
AJY3743	*MATa his3Δ1 leu2Δ0 ura3Δ0 lys2Δ0 met15Δ0 bud23Δ::KanMX imp4-S93T*	This study & (Sardana, 2013).
AJY3744	*MATa his3Δ1 leu2Δ0 ura3Δ0 lys2Δ0 met15Δ0 bud23Δ::KanMX imp4-R94S*	This study & (Sardana, 2013).
AJY3745	*MATa his3Δ1 leu2Δ0 ura3Δ0 lys2Δ0 met15Δ0 bud23Δ::KanMX imp4-N118D*	This study & (Sardana, 2013).
AJY4501	*MATa his3Δ1 leu2Δ0 ura3Δ0 lys2Δ0 met15Δ0 bud23Δ::CloNAT imp4-H159R*	This study.
AJY4502	*MATa his3Δ1 leu2Δ0 ura3Δ0 lys2Δ0 met15Δ0 bud23Δ::CloNAT utp2-L9S*	This study.
AJY4503	*MATa his3Δ1 leu2Δ0 ura3Δ0 lys2Δ0 met15Δ0 bud23Δ::CloNAT utp14-W794L*	This study.
AJY4504	*MATa his3Δ1 leu2Δ0 ura3Δ0 lys2Δ0 met15Δ0 bud23Δ::CloNAT imp4-R99L*	This study.
AJY4505	*MATa his3Δ1 leu2Δ0 ura3Δ0 lys2Δ0 met15Δ0 bud23Δ::CloNAT imp4-N121I*	This study.
AJY4506	*MATa his3Δ1 leu2Δ0 ura3Δ0 lys2Δ0 met15Δ0 bud23Δ::CloNAT imp4-Y77C*	This study.
AJY4507	*MATa his3Δ1 leu2Δ0 ura3Δ0 lys2Δ0 met15Δ0 bud23Δ::CloNAT imp4-S101W*	This study.
AJY4508	*MATa his3Δ1 leu2Δ0 ura3Δ0 lys2Δ0 met15Δ0 bud23Δ::CloNAT imp4-H208D*	This study.
AJY4509	*MATa his3Δ1 leu2Δ0 ura3Δ0 lys2Δ0 met15Δ0 bud23Δ::CloNAT imp4-R94C*	This study.
AJY4510	*MATa his3Δ1 leu2Δ0 ura3Δ0 lys2Δ0 met15Δ0 bud23Δ::CloNAT*	This study.

bioRxiv preprint doi: https://doi.org/10.1101/2020.02.05.936237; this version posted February 6, 2020. The copyright holder for this preprint (which was not certified by peer review) is the author/funder. All rights reserved. No reuse allowed without permission.

	imp4-H156D	
AJY4511	*MATa his3Δ1 leu2Δ0 ura3Δ0 lys2Δ0 met15Δ0 bud23Δ::CloNAT imp4-R99H*	This study.
AJY4512	*MATa his3Δ1 leu2Δ0 ura3Δ0 lys2Δ0 met15Δ0 bud23Δ::CloNAT imp4-R146G*	This study.
AJY4513	*MATa his3Δ1 leu2Δ0 ura3Δ0 lys2Δ0 met15Δ0 bud23Δ::CloNAT W791L*	This study.
AJY4514	*MATa his3Δ1 leu2Δ0 ura3Δ0 lys2Δ0 met15Δ0 bud23Δ::CloNAT dhr1-D408Y*	This study.
AJY4515	*MATa his3Δ1 leu2Δ0 ura3Δ0 lys2Δ0 met15Δ0 bud23Δ::CloNAT dhr1-G432R*	This study.
AJY4516	*MATa his3Δ1 leu2Δ0 ura3Δ0 lys2Δ0 met15Δ0 bud23Δ::CloNAT dhr1-S511Y*	This study.
AJY4517	*MATa his3Δ1 leu2Δ0 ura3Δ0 lys2Δ0 met15Δ0 bud23Δ::CloNAT dhr1-G434D*	This study.
AJY4518	*MATa his3Δ1 leu2Δ0 ura3Δ0 lys2Δ0 met15Δ0 bud23Δ::CloNAT dhr1-E397D*	This study.
AJY4519	*MATa his3Δ1 leu2Δ0 ura3Δ0 lys2Δ0 met15Δ0 bud23Δ::CloNAT dhr1-R596G*	This study.
AJY4520	*MATa his3Δ1 leu2Δ0 ura3Δ0 lys2Δ0 met15Δ0 bud23Δ::CloNAT dhr1-D566Y*	This study.
AJY4521	*MATa his3Δ1 leu2Δ0 ura3Δ0 lys2Δ0 met15Δ0 bud23Δ::CloNAT dhr1-A804D*	This study.
AJY4522	*MATa his3Δ1 leu2Δ0 ura3Δ0 lys2Δ0 met15Δ0 bud23Δ::CloNAT dhr1-R596S*	This study.
AJY4523	*MATa his3Δ1 leu2Δ0 ura3Δ0 lys2Δ0 met15Δ0 bud23Δ::CloNAT dhr1-M857I*	This study.
AJY4524	*MATa his3Δ1 leu2Δ0 ura3Δ0 lys2Δ0 met15Δ0 bud23Δ::CloNAT dhr1-R563M*	This study.
AJY4525	*MATa his3Δ1 leu2Δ0 ura3Δ0 lys2Δ0 met15Δ0 bud23Δ::CloNAT dhr1-R13G*	This study.
AJY4526	*MATa his3Δ1 leu2Δ0 ura3Δ0 lys2Δ0 met15Δ0 bud23Δ::CloNAT dhr1-E1037Q*	This study.
AJY4527	*MATa his3Δ1 leu2Δ0 ura3Δ0 lys2Δ0 met15Δ0 bud23Δ::CloNAT dhr1-E1037K*	This study.
AJY4529	*MATa his3Δ1 leu2Δ0 ura3Δ0 lys2Δ0 met15Δ0 bud23Δ::CloNAT*	This study.

bioRxiv preprint doi: https://doi.org/10.1101/2020.02.05.936237; this version posted February 6, 2020. The copyright holder for this preprint (which was not certified by peer review) is the author/funder. All rights reserved. No reuse allowed without permission.

	bms1-D843V	
AJY4530	*MATa his3Δ1 leu2Δ0 ura3Δ0 lys2Δ0 met15Δ0 bud23Δ::CloNAT dhr1-F594L*	This study.
AJY4531	*MATa his3Δ1 leu2Δ0 ura3Δ0 lys2Δ0 met15Δ0 bud23Δ::CloNAT rps28a-G24D*	This study.
AJY4532	*MATa his3Δ1 leu2Δ0 ura3Δ0 lys2Δ0 met15Δ0 bud23Δ::CloNAT bms1-D124Y*	This study.
AJY4533	*MATa his3Δ1 leu2Δ0 ura3Δ0 lys2Δ0 met15Δ0 bud23Δ::CloNAT bms1-A903P*	This study.
AJY4535	*MATa his3Δ1 leu2Δ0 ura3Δ0 lys2Δ0 met15Δ0 bud23Δ::CloNAT bms1-G813S*	This study.
AJY4536	*MATa his3Δ1 leu2Δ0 ura3Δ0 lys2Δ0 met15Δ0 bud23Δ::CloNAT imp4-P252L*	This study.
AJY4537	*MATa his3Δ1 leu2Δ0 ura3Δ0 lys2Δ0 met15Δ0 bud23Δ::CloNAT bms1-S1020L*	This study.
AJY4395	*MATa his3Δ1 leu2Δ0 met15Δ0ura3Δ0 ENP1-TAP::HIS3MX6 BUD23-AID-HA::OsTIR1::LEU2*	This study.
BY4741	*MATa his3Δ1 leu2Δ0 met15Δ0 ura3Δ0*	Open Biosystems
PJ69-4a	*MATa trp1-901 leu2-3,112 ura3-52 his3-200 gal4Δ gal80Δ LYS2::GAL1-HIS3 GAL2-ADE2 met2::GAL7*-lacZ	(James et al., 1996)
PJ69-4alpha	MATalpha trp1-901 leu2-3,112 ura3-52 his3-200 gal4Δ gal80Δ LYS2::GAL1-HIS3 GAL2-ADE2 met2::GAL7-lacZ	(James et al., 1996)

Table 2: Plasmids used in this study.

Plasmid	Description	Reference
pAJ2321	*GAL4AD-HA-UTP14 LEU2 2μ*	(Zhu et al., 2016)
pAJ2595	*UTP2 URA3 CEN ARS*	(Sardana et al., 2013)
pAJ2596	*utp2-A2D URA3 CEN ARS*	(Sardana et al., 2013)
pAJ2922	*GAL4BD-c-myc-DHR1 TRP1 2μ*	(Sardana et al., 2014)
pAJ2769	*GAL4BD-c-myc-IMP4 TRP1 2μ*	This study.
pAJ3332	*utp2-F149S URA3 CEN ARS*	This study.

bioRxiv preprint doi: https://doi.org/10.1101/2020.02.05.936237; this version posted February 6, 2020. The copyright holder for this preprint (which was not certified by peer review) is the author/funder. All rights reserved. No reuse allowed without permission.

pAJ3335	*utp2-L151H URA3 CEN ARS*	This study.
pAJ3347	*utp2-L148S, F149S, L151H URA3 CEN ARS*	This study.
pAJ3348	*utp2-L6P URA3 CEN ARS*	This study.
pAJ3349	*utp2-K7E URA3 CEN ARS*	This study.
pAJ3350	*utp2-L148S URA3 CEN ARS*	This study.
pAJ4093	*utp2-F58S URA3 CEN ARS*	This study.
pAJ4094	*PGAL10-UTP2 LEU2 CEN ARS*	This study.
pAJ4095	*utp2-A2D, L6P, K7E URA3 CEN ARS*	This study.
pAJ4188	*Utp2-GAL4AD-HA LEU2 2µ*	This study.
pAJ4192	*utp2-F58S-GAL4AD-HA LEU2 2µ*	This study.
pAJ4193	*utp2-L148S, F149S, L151H-GAL4AD-HA LEU2 2µ*	This study.
pAJ4194	*utp2-A2D, L6P, K7E-GAL4AD-HA LEU2 2µ*	This study.
pAJ4493	*GAL4BD-c-myc-imp4-V170F TRP1 2µ*	This study.
pAJ4494	*GAL4BD-c-myc-imp4-P252L TRP1 2µ*	This study.
pAJ4503	*GAL4BD-c-myc-DHR1-E360K, E397D, E402G, D408Y TRP1 2µ*	This study.
pAJ4513	*GAL4BD-c-myc-DHR1-R563M, D566Y, E831K, F837L TRP1 2µ*	This study.
pAJ4514	*GAL4BD-c-myc-DHR1-H593Y, R596C, E831K TRP1 2µ*	This study.
pGADT7	*GAL4AD-HA LEU2 2µ*	(Patel et al., 2007)
pGBKT7	*GAL4BD-c-myc TRP1 2µ*	(Patel et al., 2007)
pJW1662	*AtIAA17_71-114(AID*)-HA::LEU2 prADH1-OsTIR1*	(Costa et al., 2018)
pRS416	*URA3 CEN ARS*	(Sikorski and Hieter, 1989)

981

bioRxiv preprint doi: https://doi.org/10.1101/2020.02.05.936237; this version posted February 6, 2020. The copyright holder for this preprint (which was not certified by peer review) is the author/funder. All rights reserved. No reuse allowed without permission.

982 **Table 3: Oligonucleotide probes used for Northern blotting.**

Target	Sequence
+1-A0	5’ GGTCTCTCTGCTGCCGGAAATG 3’
A0-A1	5’ CCCACCTATTCCCTCTTGC 3’
A2-A3	5’ TGTTACCTCTGGGCCCCGATTG 3’
U3 snoRNA	5’ TAGATTCAATTTCGGTTTCTC 3’

983

984 Supporting information

985 Supplemental File 1 - Mass spectrometry data for Enp1-TAP affinity purifications.

986 Acknowledgments

987 This work was supported by National Institutes of Health grants GM127127, GM053655,
988 and GM108823 to AWJ, a fellowship from the University of Texas at Austin Graduate School to
989 JJB, and a fellowship from the University of Texas at Austin Office of Undergraduate Research to
990 EWE.

991 We thank S. Baserga and C. Wang for the Imp4 and Bud23 antibodies, respectively. The
992 vector pJW1662 was a gift from J. Weissman (Addgene plasmid #112050). We thank J. Ream and
993 J. Zhu for assistance with cloning, and P. Sujita for assistance with preparing samples for Illumina
994 sequencing submission. We also thank the members of the A. Johnson and Sarinay-Cenik
995 laboratories for helpful comments regarding the manuscript.

996

bioRxiv preprint doi: https://doi.org/10.1101/2020.02.05.936237; this version posted February 6, 2020. The copyright holder for this preprint (which was not certified by peer review) is the author/funder. All rights reserved. No reuse allowed without permission.

Author contributions

JJB and AWJ conceptualized, analyzed and interpreted data, and wrote the manuscript. JJB performed experiments and bioinformatic analyses. JJB, RS, EWE, and AWJ isolated and identified the suppressors of *bud23*Δ.

References

Ameismeier M, Cheng J, Berninghausen O, Beckmann R. 2018. Visualizing late states of human 40S ribosomal subunit maturation. *Nature* **558**:249–253. doi:10.1038/s41586-018-0193-0

Barandun J, Chaker-Margot M, Hunziker M, Molloy KR, Chait BT, Klinge S. 2017. The complete structure of the small-subunit processome. *Nat Struct Mol Biol* 1–36. doi:10.1038/nsmb.3472

Barandun J, Hunziker M, Klinge S. 2018. Assembly and structure of the SSU processome-a nucleolar precursor of the small ribosomal subunit. *Curr Opin Struct Biol* **49**:85–93. doi:10.1016/j.sbi.2018.01.008

Baßler J, Ahmed YL, Kallas M, Kornprobst M, Calviño FR, Gnädig M, Thoms M, Stier G, Ismail S, Kharde S, Castillo N, Griesel S, Bastuck S, Bradatsch B, Thomson E, Flemming D, Sinning I, Hurt E. 2016. Interaction network of the ribosome assembly machinery from a eukaryotic thermophile. *Protein Sci* **22**:1–50. doi:10.1002/pro.3085

Baßler J, Hurt E. 2019. Eukaryotic Ribosome Assembly. *Annu Rev Biochem* **88**:281–306. doi:10.1146/annurev-biochem-013118-110817

Ben-Shem A, Garreau de Loubresse N, Melnikov S, Jenner L, Yusupova G, Yusupov M. 2011. The structure of the eukaryotic ribosome at 3.0 Å resolution. *Science* **334**:1524–9. doi:10.1126/science.1212642

Black JJ, Wang Z, Goering LM, Johnson AW. 2018. Utp14 interaction with the Small Subunit Processome. *RNA* rna.066373.118. doi:10.1261/rna.066373.118

Boneberg FM, Brandmann T, Kobel L, van den Heuvel J, Bargsten K, Bammert L, Kutay U, Jinek M. 2019. Molecular mechanism of the RNA helicase DHX37 and its activation by UTP14A in ribosome biogenesis. *RNA* **25**:685–701. doi:10.1261/rna.069609.118

Chaker-Margot M. 2018. Assembly of the small ribosomal subunit in yeast: mechanism and regulation. *RNA* **24**:881–891. doi:10.1261/rna.066985.118

Chaker-Margot M, Barandun J, Hunziker M, Klinge S. 2017. Architecture of the yeast small subunit processome. *Science* **355**. doi:10.1126/science.aal1880

Chaker-Margot M, Hunziker M, Barandun J, Dill BD, Klinge S. 2015. Stage-specific assembly events of the 6-MDa small-subunit processome initiate eukaryotic ribosome biogenesis. *Nat Struct Mol Biol* **22**:920–3. doi:10.1038/nsmb.3111

Chen W, Xie Z, Yang F, Ye K. 2017. Stepwise assembly of the earliest precursors of large ribosomal subunits in yeast. *Nucleic Acids Res* **45**:6837–6847. doi:10.1093/nar/gkx254

Cheng J, Baßler J, Fischer P, Lau B, Kellner N, Kunze R, Griesel S, Kallas M, Berninghausen O,

bioRxiv preprint doi: https://doi.org/10.1101/2020.02.05.936237; this version posted February 6, 2020. The copyright holder for this preprint (which was not certified by peer review) is the author/funder. All rights reserved. No reuse allowed without permission.

1034 Strauss D, Beckmann R, Hurt E. 2019. Thermophile 90S Pre-ribosome Structures Reveal the
1035 Reverse Order of Co-transcriptional 18S rRNA Subdomain Integration. *Mol Cell* 1–14.
1036 doi:10.1016/j.molcel.2019.06.032
1037 Cheng J, Kellner N, Berninghausen O, Hurt E, Beckmann R. 2017. 3.2-Å-resolution structure of
1038 the 90S preribosome before A1 pre-rRNA cleavage. *Nat Struct Mol Biol* **24**:954–964.
1039 doi:10.1038/nsmb.3476
1040 Choudhury P, Hackert P, Memet I, Sloan KE, Bohnsack MT. 2018. The human RNA helicase
1041 DHX37 is required for release of the U3 snoRNP from pre-ribosomal particles. *RNA Biol*
1042 **00**:1–15. doi:10.1080/15476286.2018.1556149
1043 Colley A, Beggs JD, Tollervey D, Lafontaine DL. 2000. Dhr1p, a putative DEAH-box RNA helicase,
1044 is associated with the box C+D snoRNP U3. *Mol Cell Biol* **20**:7238–46.
1045 doi:10.1128/mcb.20.19.7238-7246.2000
1046 Costa EA, Subramanian K, Nunnari J, Weissman JS. 2018. Defining the physiological role of SRP
1047 in protein-targeting efficiency and specificity. *Science* **359**:689–692.
1048 doi:10.1126/science.aar3607
1049 Danecek P, Auton A, Abecasis G, Albers CA, Banks E, DePristo MA, Handsaker RE, Lunter G,
1050 Marth GT, Sherry ST, McVean G, Durbin R, 1000 Genomes Project Analysis Group. 2011.
1051 The variant call format and VCFtools. *Bioinformatics* **27**:2156–8.
1052 doi:10.1093/bioinformatics/btr330
1053 Delprato A, Al Kadri Y, Pérébaskine N, Monfoulet C, Henry Y, Henras AK, Fribourg S. 2014.
1054 Crucial role of the Rcl1p-Bms1p interaction for yeast pre-ribosomal RNA processing.
1055 *Nucleic Acids Res* **42**:10161–72. doi:10.1093/nar/gku682
1056 Dragon F, Gallagher JEG, Compagnone-Post PA, Mitchell BM, Porwancher KA, Wehner KA,
1057 Wormsley S, Settlage RE, Shabanowitz J, Osheim Y, Beyer AL, Hunt DF, Baserga SJ. 2002. A
1058 large nucleolar U3 ribonucleoprotein required for 18S ribosomal RNA biogenesis. *Nature*
1059 **417**:967–70. doi:10.1038/nature00769
1060 Ferreira-Cerca S, Kiburu I, Thomson E, LaRonde N, Hurt E. 2014. Dominant Rio1 kinase/ATPase
1061 catalytic mutant induces trapping of late pre-40S biogenesis factors in 80S-like ribosomes.
1062 *Nucleic Acids Res* **42**:8635–47. doi:10.1093/nar/gku542
1063 Fischer U, Schäuble N, Schütz S, Altvater M, Chang Y, Faza MB, Panse VG. 2015. A non-canonical
1064 mechanism for Crm1-export cargo complex assembly. *Elife* **4**:1–20.
1065 doi:10.7554/eLife.05745
1066 Gallagher JEG, Baserga SJ. 2004. Two-hybrid Mpp10p interaction-defective Imp4 proteins are
1067 not interaction defective in vivo but do confer specific pre-rRNA processing defects in
1068 *Saccharomyces cerevisiae*. *Nucleic Acids Res* **32**:1404–13. doi:10.1093/nar/gkh318
1069 Gelperin D, Horton L, Beckman J, Hensold J, Lemmon SK. 2001. Bms1p, a novel GTP-binding
1070 protein, and the related Tsr1p are required for distinct steps of 40S ribosome biogenesis in
1071 yeast. *RNA* **7**:1268–83. doi:10.1017/S1355838201013073
1072 Gérczei T, Correll CC. 2004. Imp3p and Imp4p mediate formation of essential U3-precursor
1073 rRNA (pre-rRNA) duplexes, possibly to recruit the small subunit processome to the pre-
1074 rRNA. *Proc Natl Acad Sci U S A* **101**:15301–6. doi:10.1073/pnas.0406819101
1075 Ghaemmaghami S, Huh W-K, Bower K, Howson RW, Belle a, Dephoure N, O'Shea EK, Weissman
1076 JS. 2003. Global analysis of protein expression in yeast. *Nature* **425**:737–741.
1077 doi:10.1038/nature02046\nnature02046 [pii]

bioRxiv preprint doi: https://doi.org/10.1101/2020.02.05.936237; this version posted February 6, 2020. The copyright holder for this preprint (which was not certified by peer review) is the author/funder. All rights reserved. No reuse allowed without permission.

1078 Hunziker M, Barandun J, Buzovetsky O, Steckler C, Molina H, Klinge S. 2019. Conformational
1079 switches control early maturation of the eukaryotic small ribosomal subunit. *Elife* **8**:1–16.
1080 doi:10.7554/eLife.45185
1081 Hunziker M, Barandun J, Petfalski E, Tan D, Delan-Forino C, Molloy KR, Kim KH, Dunn-Davies H,
1082 Shi Y, Chaker-Margot M, Chait BT, Walz T, Tollervey D, Klinge S. 2016. UtpA and UtpB
1083 chaperone nascent pre-ribosomal RNA and U3 snoRNA to initiate eukaryotic ribosome
1084 assembly. *Nat Commun* **7**:12090. doi:10.1038/ncomms12090
1085 James P, Halladay J, Craig E a. 1996. Genomic libraries and a host strain designed for highly
1086 efficient two-hybrid selection in yeast. *Genetics* **144**:1425–36.
1087 Karbstein K, Doudna JA. 2006. GTP-dependent formation of a ribonucleoprotein subcomplex
1088 required for ribosome biogenesis. *J Mol Biol* **356**:432–43. doi:10.1016/j.jmb.2005.11.052
1089 Karbstein K, Jonas S, Doudna JA. 2005. An essential GTPase promotes assembly of preribosomal
1090 RNA processing complexes. *Mol Cell* **20**:633–43. doi:10.1016/j.molcel.2005.09.017
1091 Klinge S, Woolford JL. 2019. Ribosome assembly coming into focus. *Nat Rev Mol Cell Biol*
1092 **20**:116–131. doi:10.1038/s41580-018-0078-y
1093 Kos M, Tollervey D. 2010. Yeast pre-rRNA processing and modification occur cotranscriptionally.
1094 *Mol Cell* **37**:809–20. doi:10.1016/j.molcel.2010.02.024
1095 Kressler D, Hurt E, Baßler J. 2017. A Puzzle of Life: Crafting Ribosomal Subunits. *Trends Biochem*
1096 *Sci* **42**:640–654. doi:10.1016/j.tibs.2017.05.005
1097 Lackmann F, Belikov S, Burlacu E, Granneman S, Wieslander L. 2018. Maturation of the 90S pre-
1098 ribosome requires Mrd1 dependent U3 snoRNA and 35S pre-rRNA structural
1099 rearrangements. *Nucleic Acids Res* **46**:3692–3706. doi:10.1093/nar/gky036
1100 Langmead B, Salzberg SL. 2012. Fast gapped-read alignment with Bowtie 2. *Nat Methods* **9**:357–
1101 9. doi:10.1038/nmeth.1923
1102 Lee SJ, Baserga SJ. 1999. Imp3p and Imp4p, two specific components of the U3 small nucleolar
1103 ribonucleoprotein that are essential for pre-18S rRNA processing. *Mol Cell Biol* **19**:5441–
1104 52. doi:10.1128/MCB.19.8.5441
1105 Létoquart J, Huvelle E, Wacheul L, Bourgeois G, Zorbas C, Graille M, Heurgué-Hamard V,
1106 Lafontaine DLJ. 2014. Structural and functional studies of Bud23-Trm112 reveal 18S rRNA
1107 N7-G1575 methylation occurs on late 40S precursor ribosomes. *Proc Natl Acad Sci U S A*
1108 **111**:E5518-26. doi:10.1073/pnas.1413089111
1109 Li H, Handsaker B, Wysoker A, Fennell T, Ruan J, Homer N, Marth G, Abecasis G, Durbin R, 1000
1110 Genome Project Data Processing Subgroup. 2009. The Sequence Alignment/Map format
1111 and SAMtools. *Bioinformatics* **25**:2078–9. doi:10.1093/bioinformatics/btp352
1112 Liu PC, Thiele DJ. 2001. Novel stress-responsive genes EMG1 and NOP14 encode conserved,
1113 interacting proteins required for 40S ribosome biogenesis. *Mol Biol Cell* **12**:3644–57.
1114 doi:10.1091/mbc.12.11.3644
1115 Maracci C, Rodnina M V. 2016. Review: Translational GTPases. *Biopolymers* **105**:463–75.
1116 doi:10.1002/bip.22832
1117 Musalgaonkar S, Black JJ, Johnson A. 2019. The L1 stalk is required for efficient export of
1118 nascent large ribosomal subunits in yeast. *RNA* rna.071811.119.
1119 doi:10.1261/rna.071811.119
1120 Narasimhan V, Danecek P, Scally A, Xue Y, Tyler-Smith C, Durbin R. 2016. BCFtools/RoH: a
1121 hidden Markov model approach for detecting autozygosity from next-generation

bioRxiv preprint doi: https://doi.org/10.1101/2020.02.05.936237; this version posted February 6, 2020. The copyright holder for this preprint (which was not certified by peer review) is the author/funder. All rights reserved. No reuse allowed without permission.

sequencing data. *Bioinformatics* **32**:1749–51. doi:10.1093/bioinformatics/btw044

Nishimura K, Fukagawa T, Takisawa H, Kakimoto T, Kanemaki M. 2009. An auxin-based degron system for the rapid depletion of proteins in nonplant cells. *Nat Methods* **6**:917–22. doi:10.1038/nmeth.1401

Nissen P, Thirup S, Kjeldgaard M, Nyborg J. 1999. The crystal structure of Cys-tRNACys-EF-Tu-GDPNP reveals general and specific features in the ternary complex and in tRNA. *Structure* **7**:143–56.

Noeske J, Wasserman MR, Terry DS, Altman RB, Blanchard SC, Cate JHD. 2015. High-resolution structure of the *Escherichia coli* ribosome. *Nat Struct Mol Biol* **22**:336–41. doi:10.1038/nsmb.2994

Oeffinger M, Wei KE, Rogers R, DeGrasse JA, Chait BT, Aitchison JD, Rout MP. 2007. Comprehensive analysis of diverse ribonucleoprotein complexes. *Nat Methods* **4**:951–6. doi:10.1038/nmeth1101

Patel SS, Belmont BJ, Sante JM, Rexach MF. 2007. Natively unfolded nucleoporins gate protein diffusion across the nuclear pore complex. *Cell* **129**:83–96. doi:10.1016/j.cell.2007.01.044

Roychowdhury A, Joret C, Bourgeois G, Heurgué-Hamard V, Lafontaine DLJ, Graille M. 2019. The DEAH-box RNA helicase Dhr1 contains a remarkable carboxyl terminal domain essential for small ribosomal subunit biogenesis. *Nucleic Acids Res*. doi:10.1093/nar/gkz529

Sá-Moura B, Kornprobst M, Kharde S, Ahmed YL, Stier G, Kunze R, Sinning I, Hurt E. 2017. Mpp10 represents a platform for the interaction of multiple factors within the 90S pre-ribosome. *PLoS One* **12**:e0183272. doi:10.1371/journal.pone.0183272

Sardana R. 2013. From knobs to a central pseudoknot: understanding 40S ribosomal subunit biogenesis through Bud23. The University of Texas at Austin.

Sardana R, Johnson AW. 2012. The methyltransferase adaptor protein Trm112 is involved in biogenesis of both ribosomal subunits. *Mol Biol Cell* **23**:4313–22. doi:10.1091/mbc.E12-05-0370

Sardana R, Liu X, Granneman S, Zhu J, Gill M, Papoulas O, Marcotte EM, Tollervey D, Correll CC, Johnson AW. 2015. The DEAH-box helicase Dhr1 dissociates U3 from the pre-rRNA to promote formation of the central pseudoknot. *PLoS Biol* **13**:e1002083. doi:10.1371/journal.pbio.1002083

Sardana R, White JP, Johnson AW. 2013. The rRNA methyltransferase Bud23 shows functional interaction with components of the SSU processome and RNase MRP. *RNA* **19**:828–40. doi:10.1261/rna.037671.112

Sardana R, Zhu J, Gill M, Johnson AW. 2014. Physical and functional interaction between the methyltransferase Bud23 and the essential DEAH-box RNA helicase Ecm16. *Mol Cell Biol* **34**:2208–20. doi:10.1128/MCB.01656-13

Schäfer T, Strauss D, Petfalski E, Tollervey D, Hurt E. 2003. The path from nucleolar 90S to cytoplasmic 40S pre-ribosomes. *EMBO J* **22**:1370–80. doi:10.1093/emboj/cdg121

Sikorski RS, Hieter P. 1989. A system of shuttle vectors and yeast host strains designed for efficient manipulation of DNA in *Saccharomyces cerevisiae*. *Genetics* **122**:19–27. doi:0378111995000377 [pii]

Sloan KE, Warda AS, Sharma S, Entian K-D, Lafontaine DLJ, Bohnsack MT. 2016. Tuning the ribosome: The influence of rRNA modification on eukaryotic ribosome biogenesis and function. *RNA Biol* **408**:1–16. doi:10.1080/15476286.2016.1259781

bioRxiv preprint doi: https://doi.org/10.1101/2020.02.05.936237; this version posted February 6, 2020. The copyright holder for this preprint (which was not certified by peer review) is the author/funder. All rights reserved. No reuse allowed without permission.

1166 Small EC, Leggett SR, Winans AA, Staley JP. 2006. The EF-G-like GTPase Snu114p regulates
1167 spliceosome dynamics mediated by Brr2p, a DExD/H box ATPase. *Mol Cell* **23**:389–99.
1168 doi:10.1016/j.molcel.2006.05.043
1169 Song H, Parsons MR, Rowsell S, Leonard G, Phillips SEV. 1999. Crystal structure of intact
1170 elongation factor EF-Tu from Escherichia coli in GDP conformation at 2.05 A resolution. *J*
1171 *Mol Biol* **285**:1245–56. doi:10.1006/jmbi.1998.2387
1172 Sun Q, Zhu X, Qi J, An W, Lan P, Tan D, Chen R, Wang B, Zheng S, Zhang C, Chen X, Zhang W,
1173 Chen J, Dong M-Q, Ye K. 2017. Molecular architecture of the 90S small subunit pre-
1174 ribosome. *Elife* **6**:e22086. doi:10.7554/eLife.22086
1175 Tomecki R, Sikorski PJ, Zakrzewska-Placzek M. 2017. Comparison of preribosomal RNA
1176 processing pathways in yeast, plant and human cells - focus on coordinated action of
1177 endo- and exoribonucleases. *FEBS Lett* **591**:1801–1850. doi:10.1002/1873-3468.12682
1178 Tong AHY, Evangelista M, Parsons AB, Xu H, Bader GD, Pagé N, Robinson M, Raghibizadeh S,
1179 Hogue CWV, Bussey H, Andrews B, Tyers M, Boone C. 2001. Systematic genetic analysis
1180 with ordered arrays of yeast deletion mutants. *Science* **294**:2364–8.
1181 doi:10.1126/science.1065810
1182 Vincent NG, Charette JM, Baserga SJ. 2018. The SSU processome interactome in *Saccharomyces*
1183 *cerevisiae* reveals novel protein subcomplexes. *RNA* **24**:77–89.
1184 doi:10.1261/rna.062927.117
1185 Wegierski T, Billy E, Nasr F, Filipowicz W. 2001. Bms1p, a G-domain-containing protein,
1186 associates with Rcl1p and is required for 18S rRNA biogenesis in yeast. *RNA* **7**:1254–67.
1187 doi:10.1017/S1355838201012079
1188 Wells GR, Weichmann F, Colvin D, Sloan KE, Kudla G, Tollervey D, Watkins NJ, Schneider C.
1189 2016. The PIN domain endonuclease Utp24 cleaves pre-ribosomal RNA at two coupled
1190 sites in yeast and humans. *Nucleic Acids Res* gkw213. doi:10.1093/nar/gkw213
1191 White J, Li Z, Sardana R, Bujnicki JM, Marcotte EM, Johnson AW. 2008. Bud23 methylates
1192 G1575 of 18S rRNA and is required for efficient nuclear export of pre-40S subunits. *Mol*
1193 *Cell Biol* **28**:3151–61. doi:10.1128/MCB.01674-07
1194 Winzeler EA, Shoemaker DD, Astromoff A, Liang H, Anderson K, Andre B, Bangham R, Benito R,
1195 Boeke JD, Bussey H, Chu AM, Connelly C, Davis K, Dietrich F, Dow SW, El Bakkoury M,
1196 Foury F, Friend SH, Gentalen E, Giaever G, Hegemann JH, Jones T, Laub M, Liao H,
1197 Liebundguth N, Lockhart DJ, Lucau-Danila A, Lussier M, M'Rabet N, Menard P, Mittmann
1198 M, Pai C, Rebischung C, Revuelta JL, Riles L, Roberts CJ, Ross-MacDonald P, Scherens B,
1199 Snyder M, Sookhai-Mahadeo S, Storms RK, Véronneau S, Voet M, Volckaert G, Ward TR,
1200 Wysocki R, Yen GS, Yu K, Zimmermann K, Philippsen P, Johnston M, Davis RW. 1999.
1201 Functional characterization of the *S. cerevisiae* genome by gene deletion and parallel
1202 analysis. *Science* **285**:901–6. doi:10.1126/science.285.5429.901
1203 Wittinghofer A, Vetter IR. 2011. Structure-function relationships of the G domain, a canonical
1204 switch motif. *Annu Rev Biochem* **80**:943–71. doi:10.1146/annurev-biochem-062708-
1205 134043
1206 Zhang L, Wu C, Cai G, Chen S, Ye K. 2016. Stepwise and dynamic assembly of the earliest
1207 precursors of small ribosomal subunits in yeast. *Genes Dev* **30**:718–32.
1208 doi:10.1101/gad.274688.115
1209 Zhu J, Liu X, Anjos M, Correll CC, Johnson AW. 2016. Utp14 Recruits and Activates the RNA

bioRxiv preprint doi: https://doi.org/10.1101/2020.02.05.936237; this version posted February 6, 2020. The copyright holder for this preprint (which was not certified by peer review) is the author/funder. All rights reserved. No reuse allowed without permission.

1210 Helicase Dhr1 To Undock U3 snoRNA from the Preribosome. *Mol Cell Biol* **36**:965–78.
1211 doi:10.1128/MCB.00773-15
1212 Zorbas C, Nicolas E, Wacheul L, Huvelle E, Heurgué-Hamard V, Lafontaine DLJ. 2015. The human
1213 18S rRNA base methyltransferases DIMT1L and WBSCR22-TRMT112 but not rRNA
1214 modification are required for ribosome biogenesis. *Mol Biol Cell* **26**:2080–95.
1215 doi:10.1091/mbc.E15-02-0073
1216

bioRxiv preprint doi: https://doi.org/10.1101/2020.02.05.936237; this version posted February 6, 2020. The copyright holder for this preprint (which was not certified by peer review) is the author/funder. All rights reserved. No reuse allowed without permission.

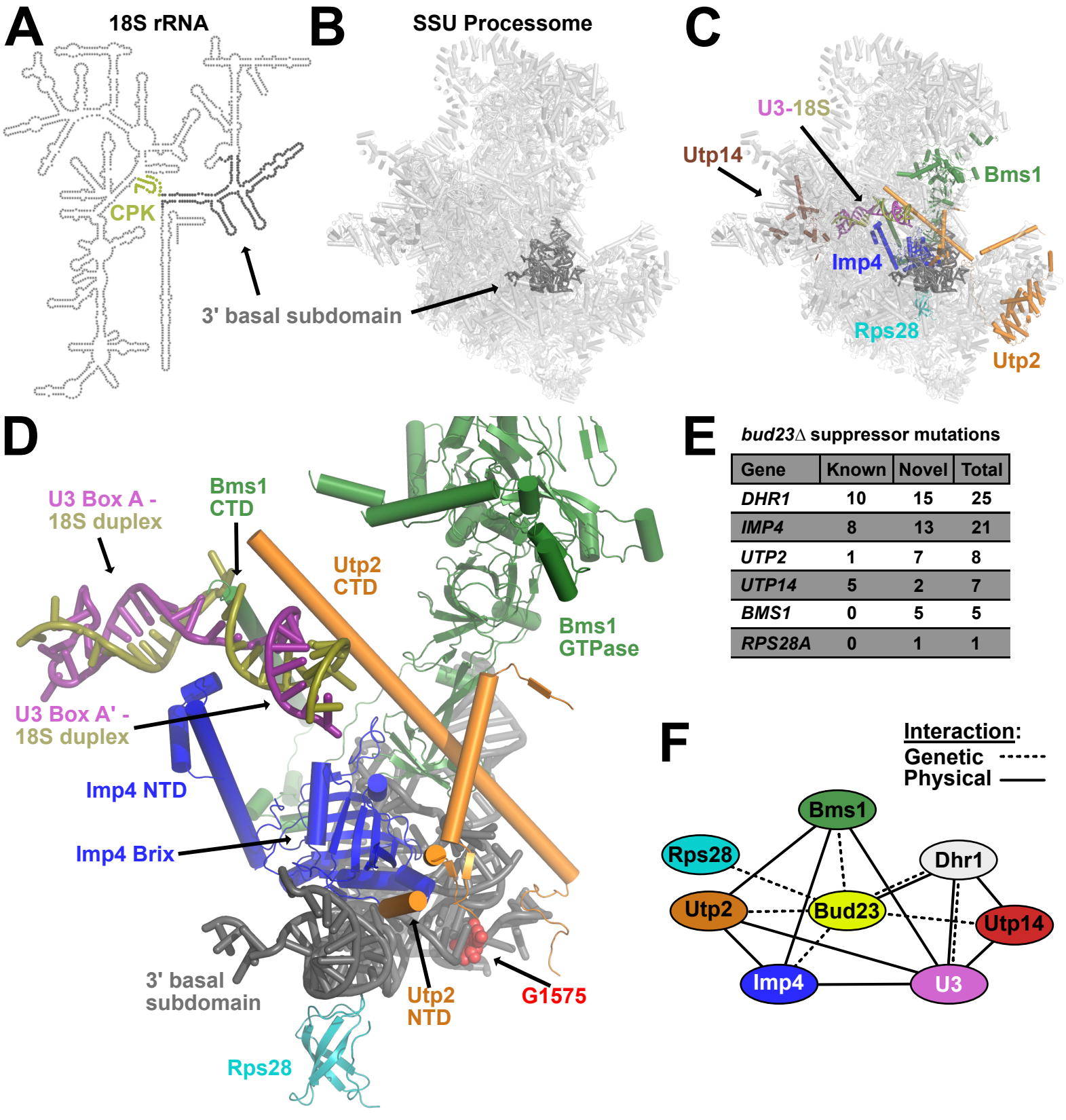

Gene	Known	Novel	Total
DHR1	10	15	25
IMP4	8	13	21
UTP2	1	7	8
UTP14	5	2	7
BMS1	0	5	5
RPS28A	0	1	1

Figure 1, Black, et al 2020

bioRxiv preprint doi: https://doi.org/10.1101/2020.02.05.936237; this version posted February 6, 2020. The copyright holder for this preprint (which was not certified by peer review) is the author/funder. All rights reserved. No reuse allowed without permission.

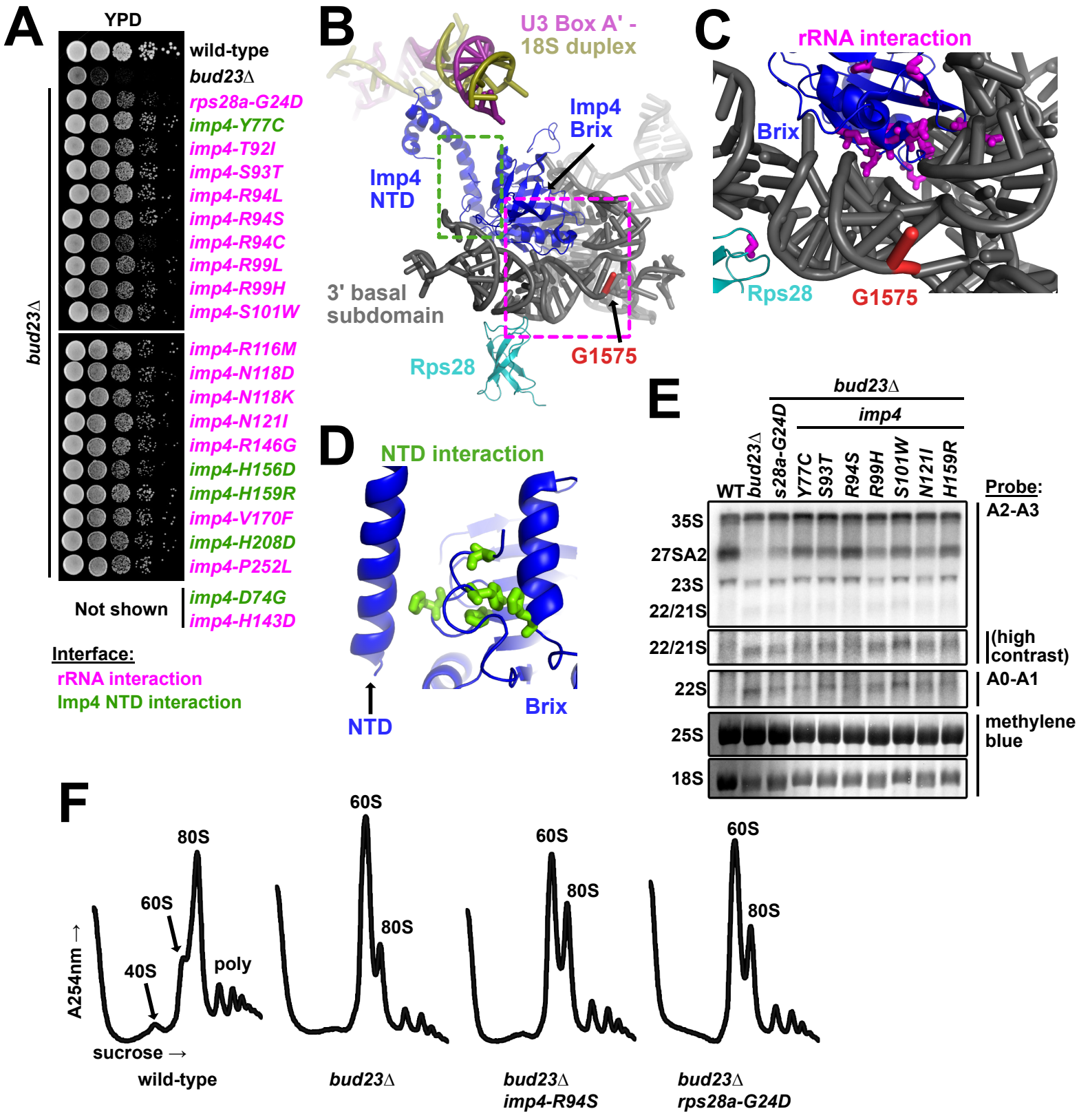

Figure 2, Black, et al 2020

bioRxiv preprint doi: https://doi.org/10.1101/2020.02.05.936237; this version posted February 6, 2020. The copyright holder for this preprint (which was not certified by peer review) is the author/funder. All rights reserved. No reuse allowed without permission.

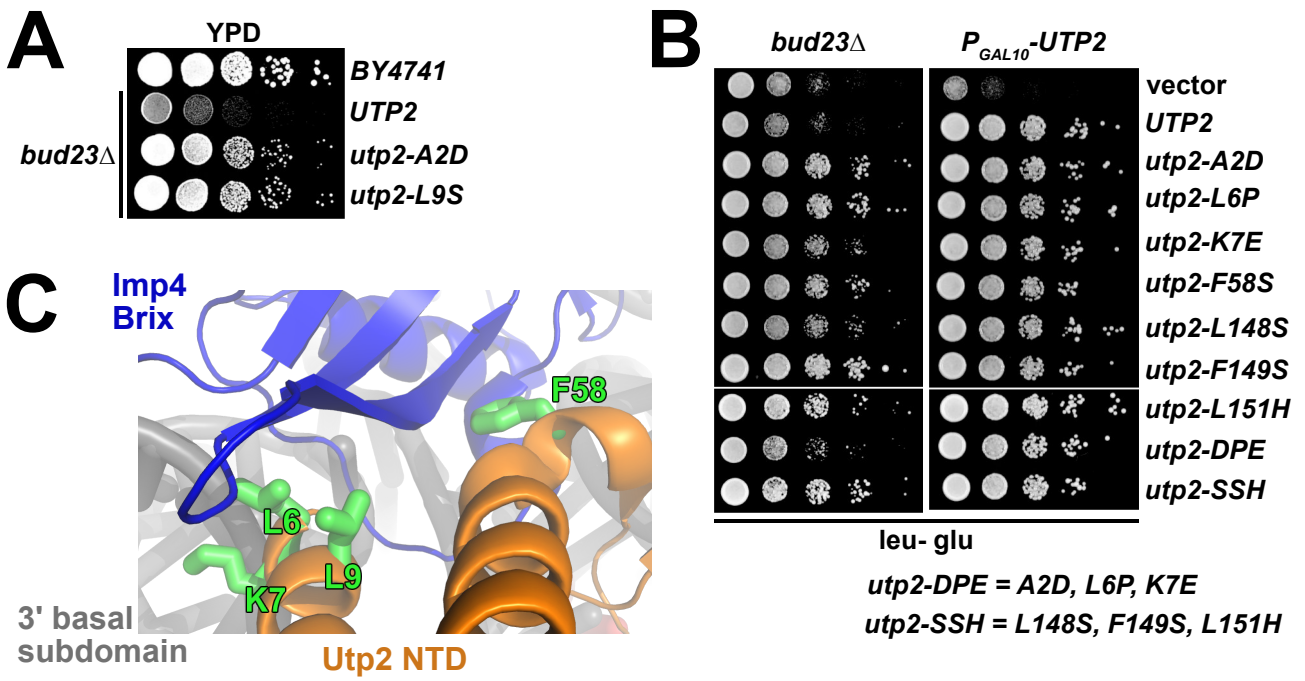

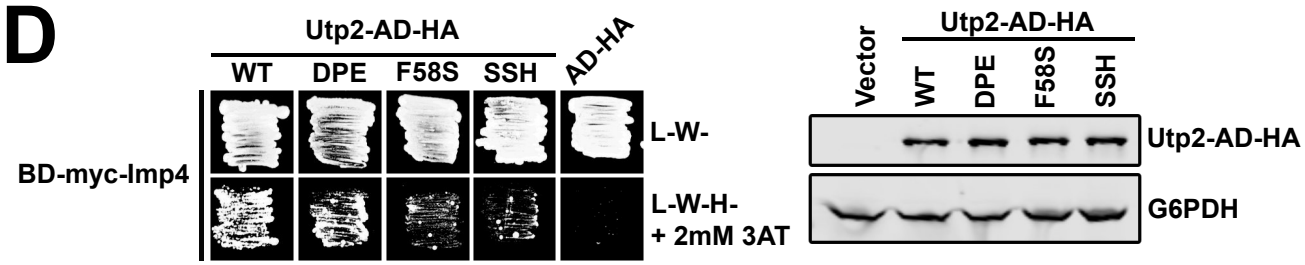

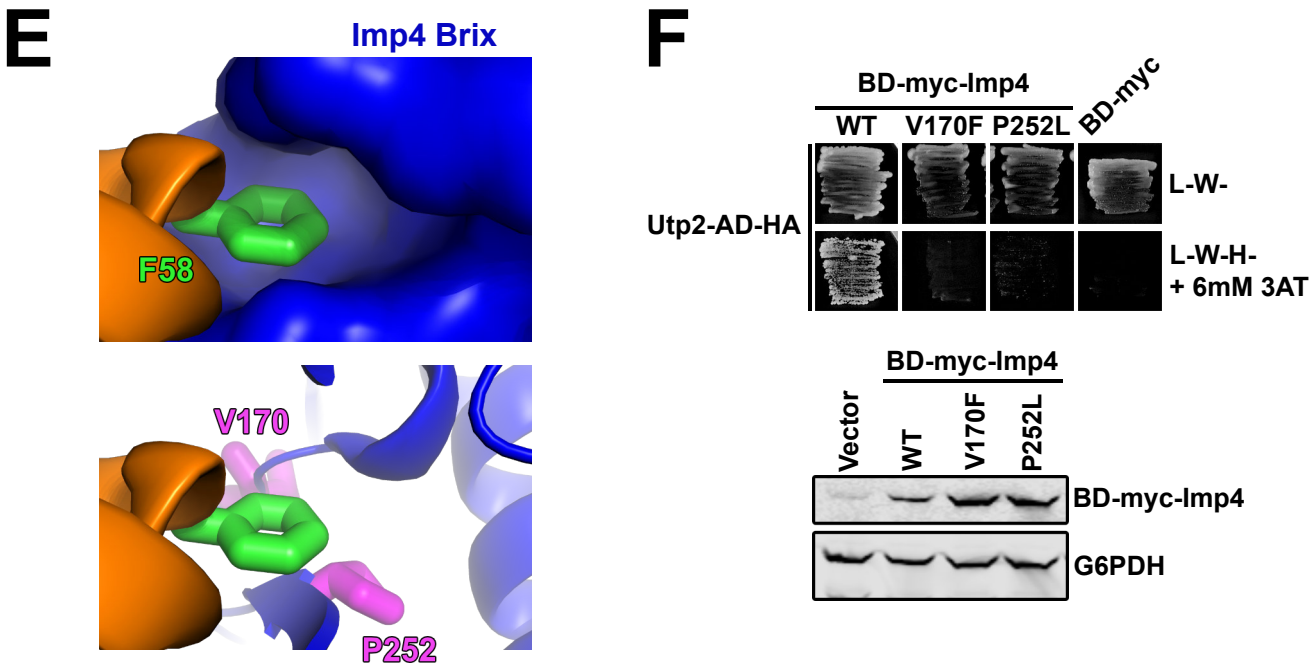

Figure 3, Black, et al 2020

bioRxiv preprint doi: https://doi.org/10.1101/2020.02.05.936237; this version posted February 6, 2020. The copyright holder for this preprint (which was not certified by peer review) is the author/funder. All rights reserved. No reuse allowed without permission.

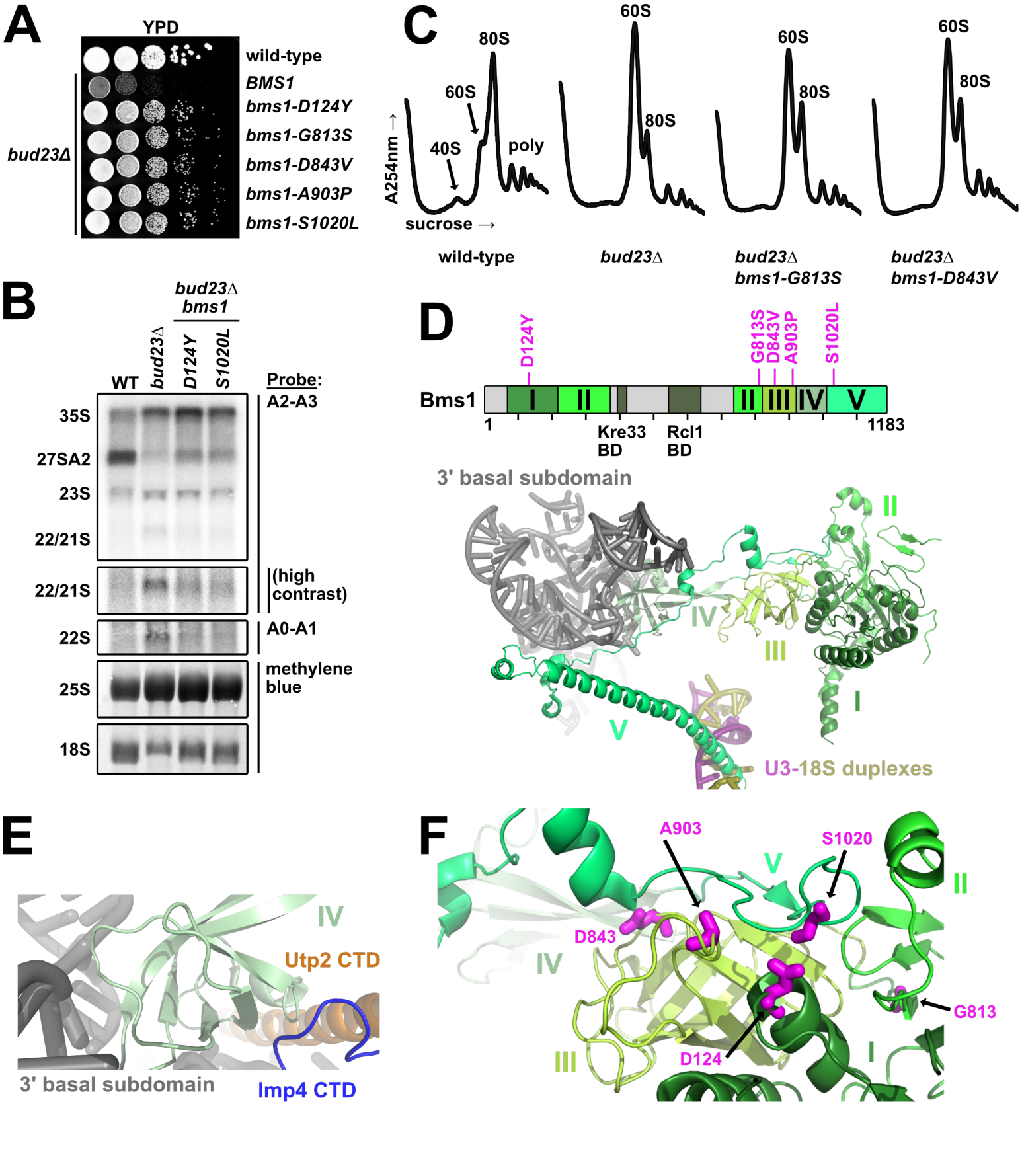

Figure 4, Black, et al 2020

bioRxiv preprint doi: https://doi.org/10.1101/2020.02.05.936237; this version posted February 6, 2020. The copyright holder for this preprint (which was not certified by peer review) is the author/funder. All rights reserved. No reuse allowed without permission.

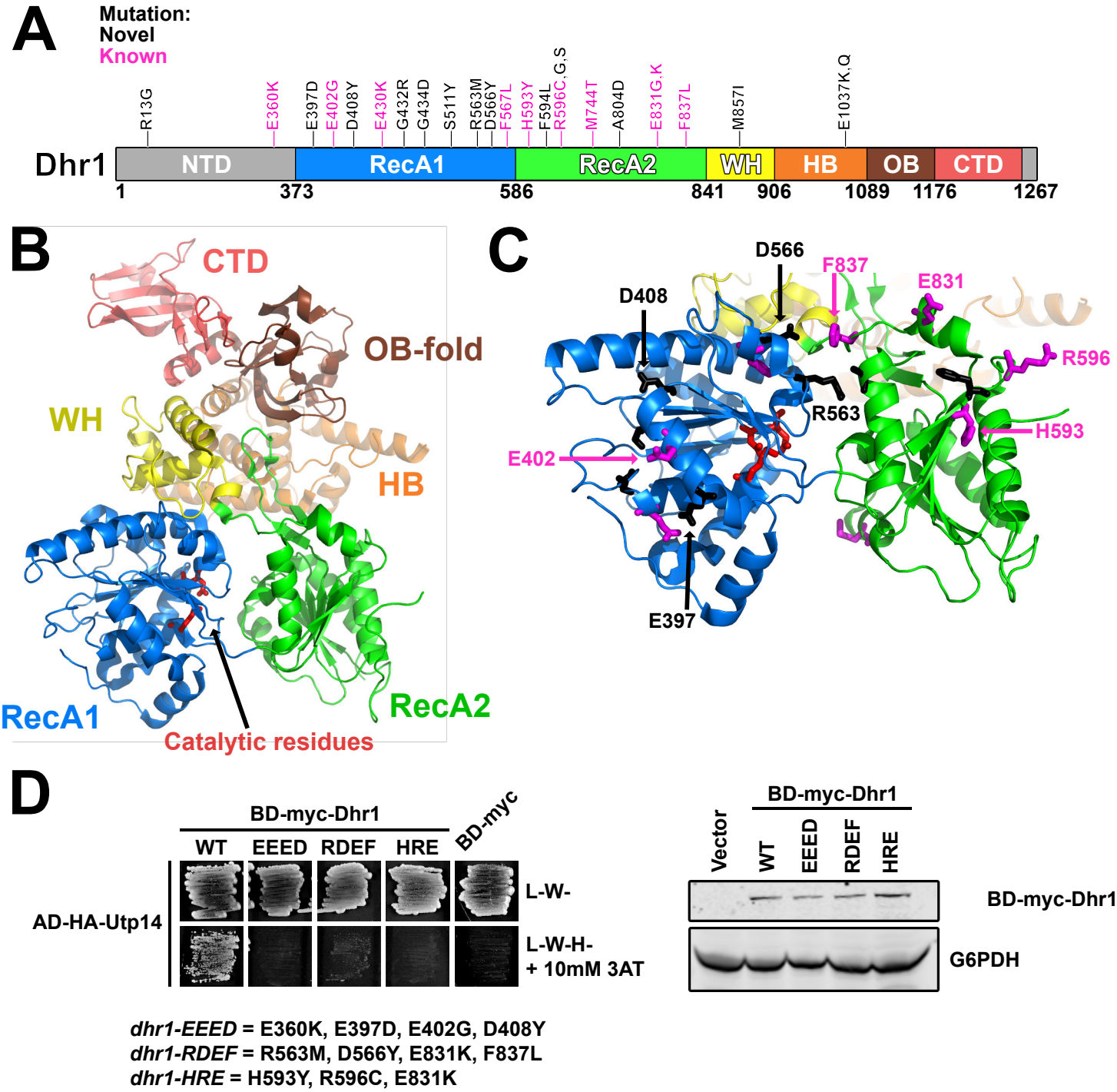

dhr1-EEED = E360K, E397D, E402G, D408Y
dhr1-RDEF = R563M, D566Y, E831K, F837L
dhr1-HRE = H593Y, R596C, E831K

Figure 5, Black, et al 2020

bioRxiv preprint doi: https://doi.org/10.1101/2020.02.05.936237; this version posted February 6, 2020. The copyright holder for this preprint
(which was not certified by peer review) is the author/funder. All rights reserved. No reuse allowed without permission.

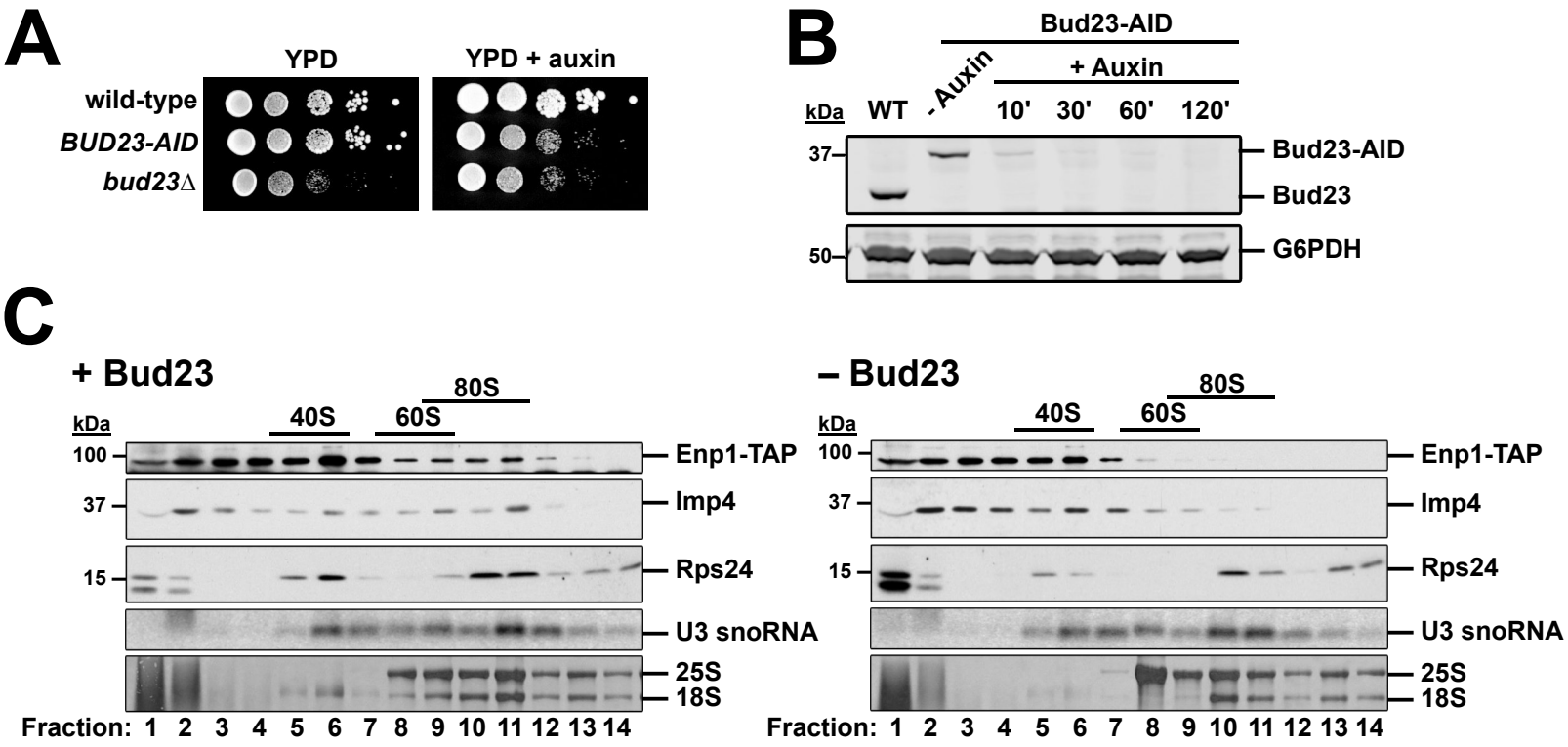

Figure 6, Black, et al 2020

bioRxiv preprint doi: https://doi.org/10.1101/2020.02.05.936237; this version posted February 6, 2020. The copyright holder for this preprint (which was not certified by peer review) is the author/funder. All rights reserved. No reuse allowed without permission.

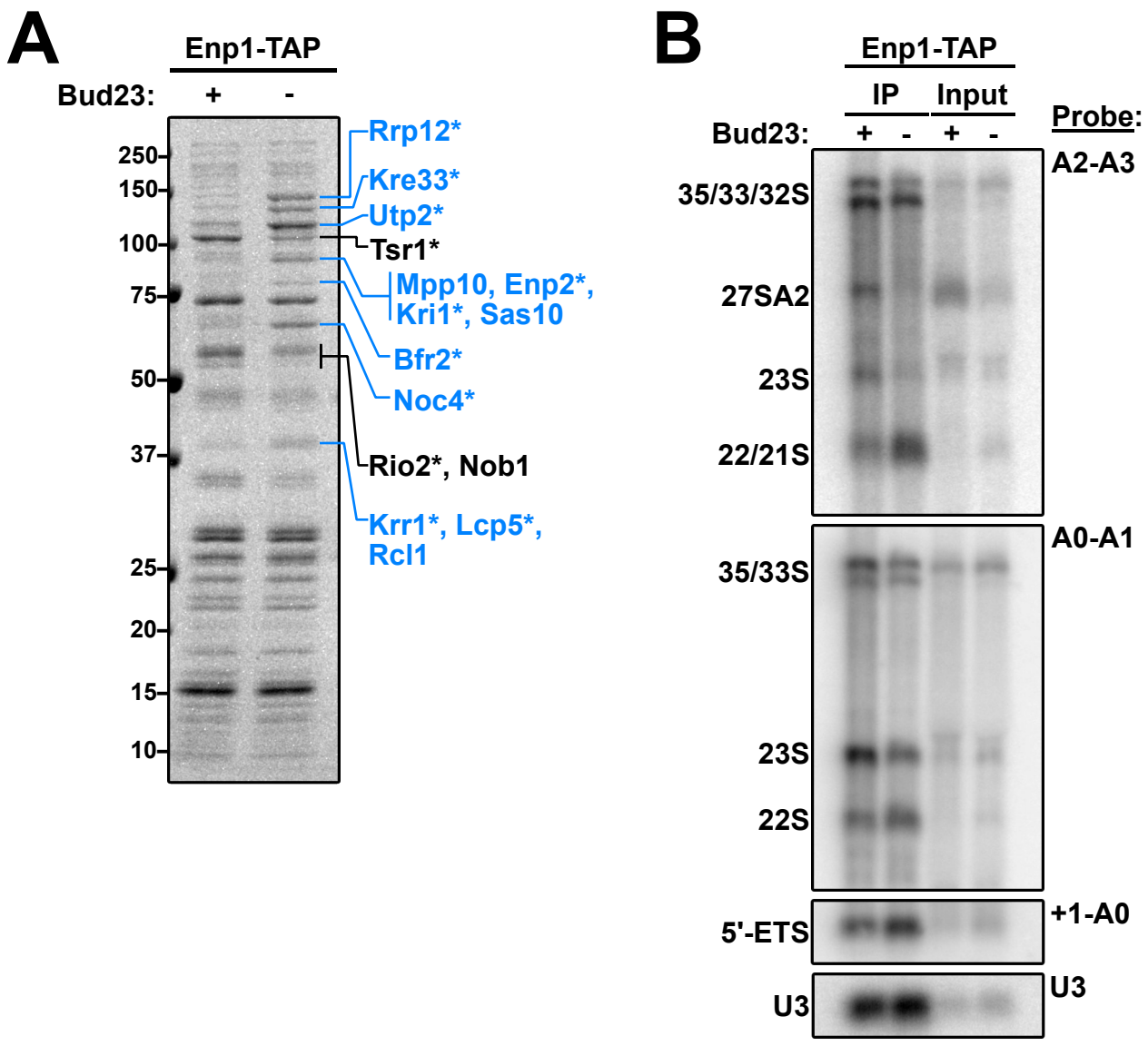

Figure 7, Black, et al 2020

bioRxiv preprint doi: https://doi.org/10.1101/2020.02.05.936237; this version posted February 6, 2020. The copyright holder for this preprint (which was not certified by peer review) is the author/funder. All rights reserved. No reuse allowed without permission.

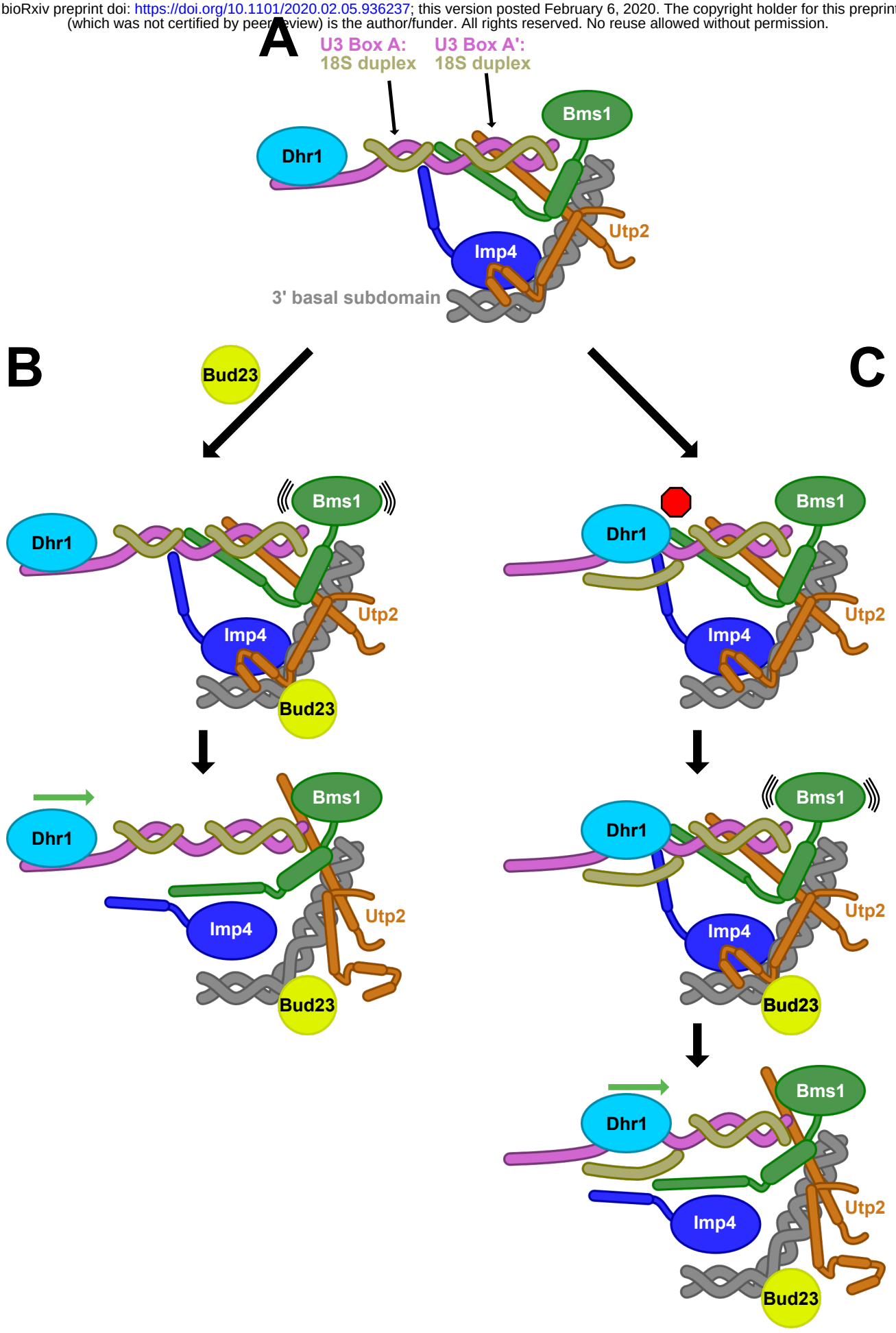

Figure 8, Black, et al 2020

bioRxiv preprint doi: https://doi.org/10.1101/2020.02.05.936237; this version posted February 6, 2020. The copyright holder for this preprint (which was not certified by peer review) is the author/funder. All rights reserved. No reuse allowed without permission.

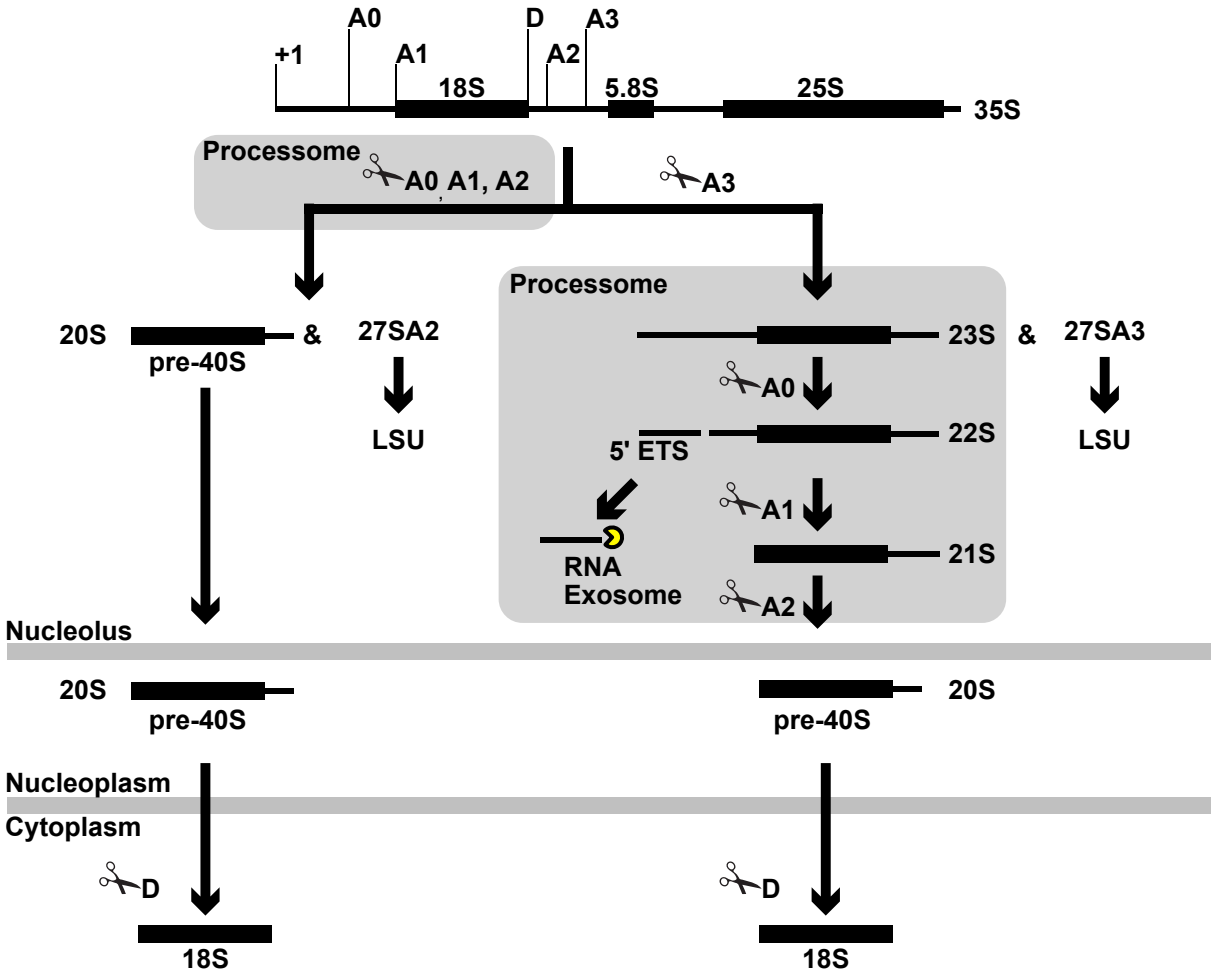

Figure S1, Black, et al 2020

bioRxiv preprint doi: https://doi.org/10.1101/2020.02.05.936237; this version posted February 6, 2020. The copyright holder for this preprint (which was not certified by peer review) is the author/funder. All rights reserved. No reuse allowed without permission.

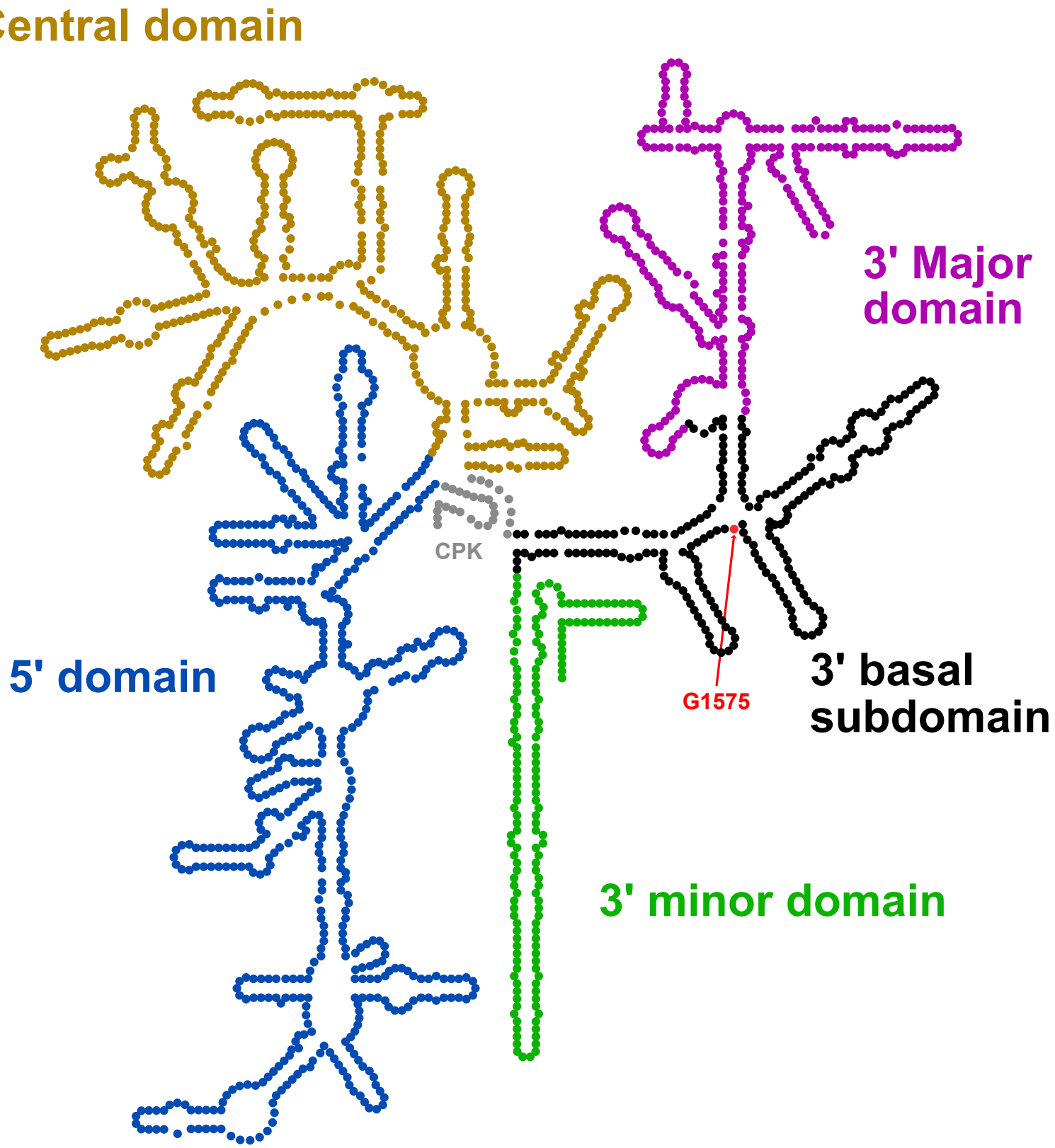

A 3D-based secondary structure, generated by RiboVision.

Figure S2, Black, et al 2020

bioRxiv preprint doi: https://doi.org/10.1101/2020.02.05.936237; this version posted February 6, 2020. The copyright holder for this preprint (which was not certified by peer review) is the author/funder. All rights reserved. No reuse allowed without permission.

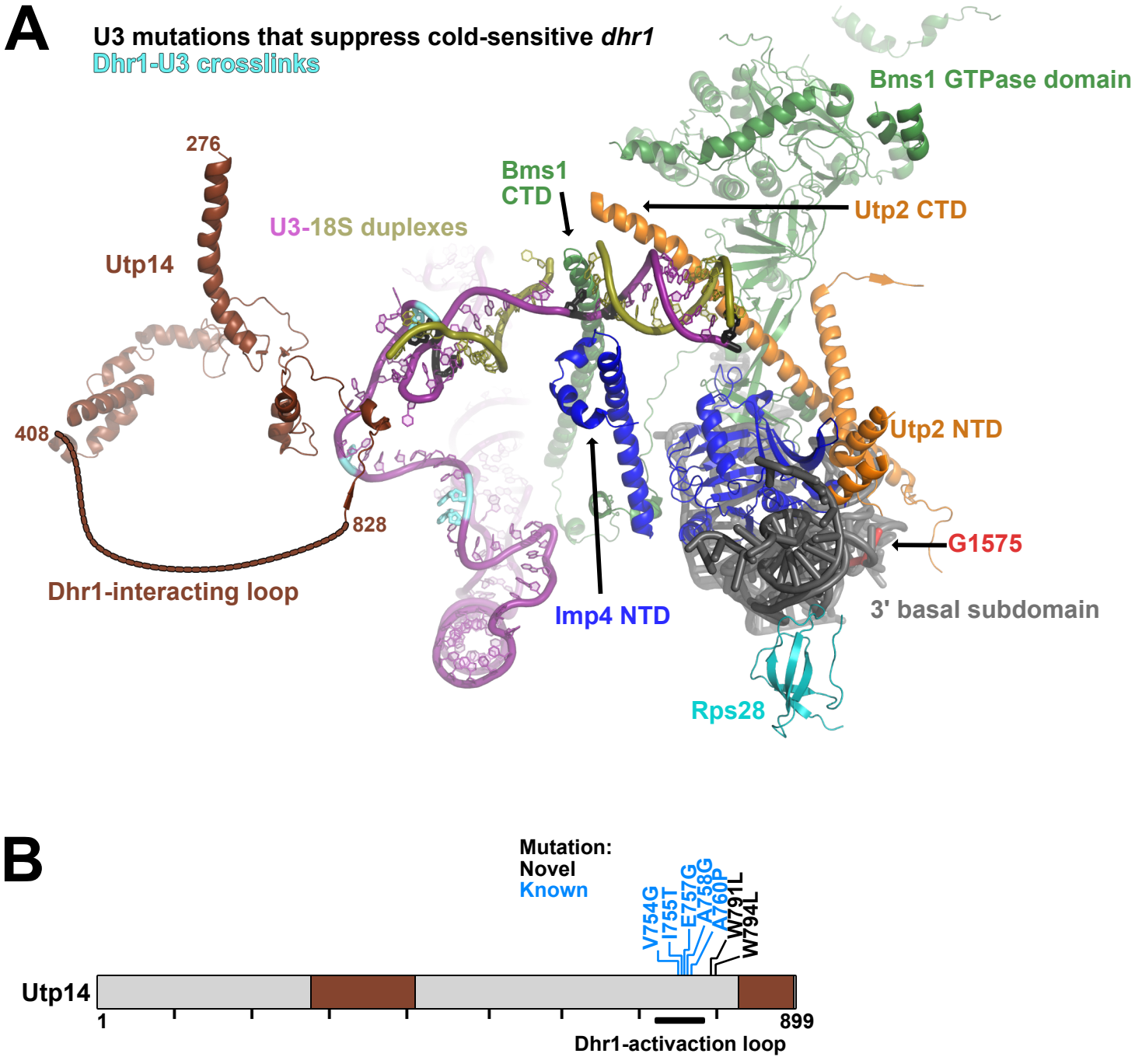

Figure S3, Black, et al 2020

bioRxiv preprint doi: https://doi.org/10.1101/2020.02.05.936237; this version posted February 6, 2020. The copyright holder for this preprint (which was not certified by peer review) is the author/funder. All rights reserved. No reuse allowed without permission.

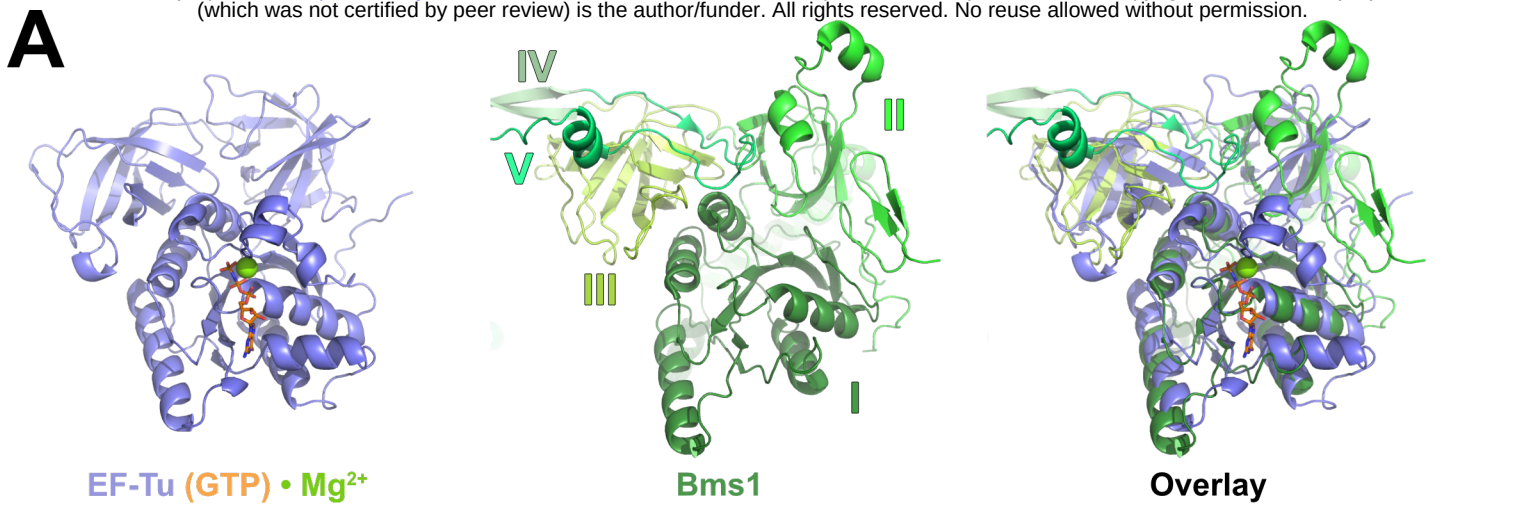

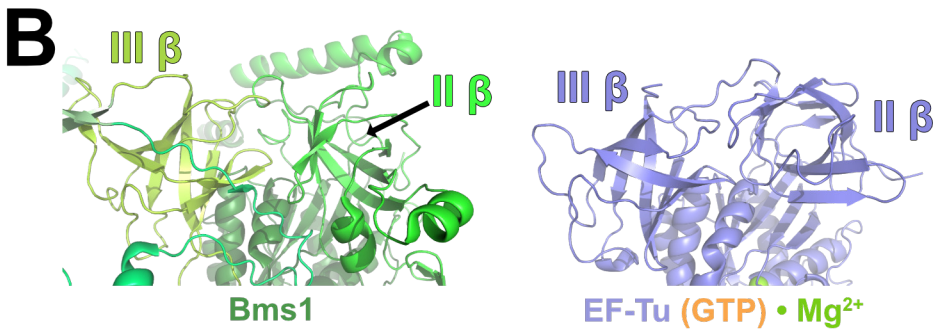

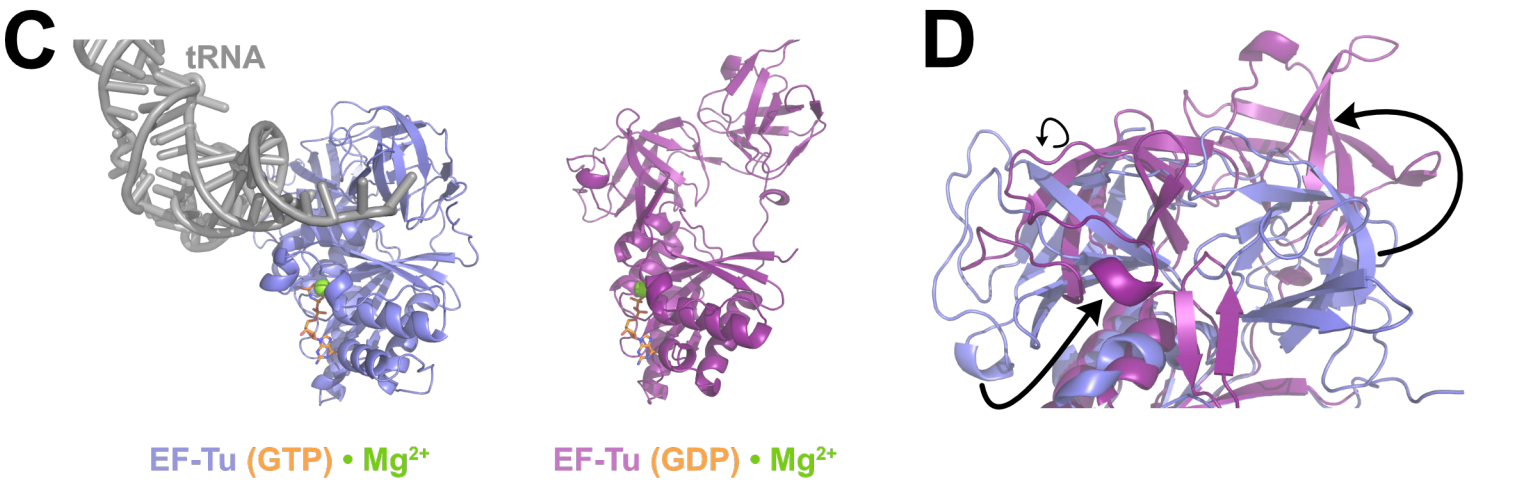

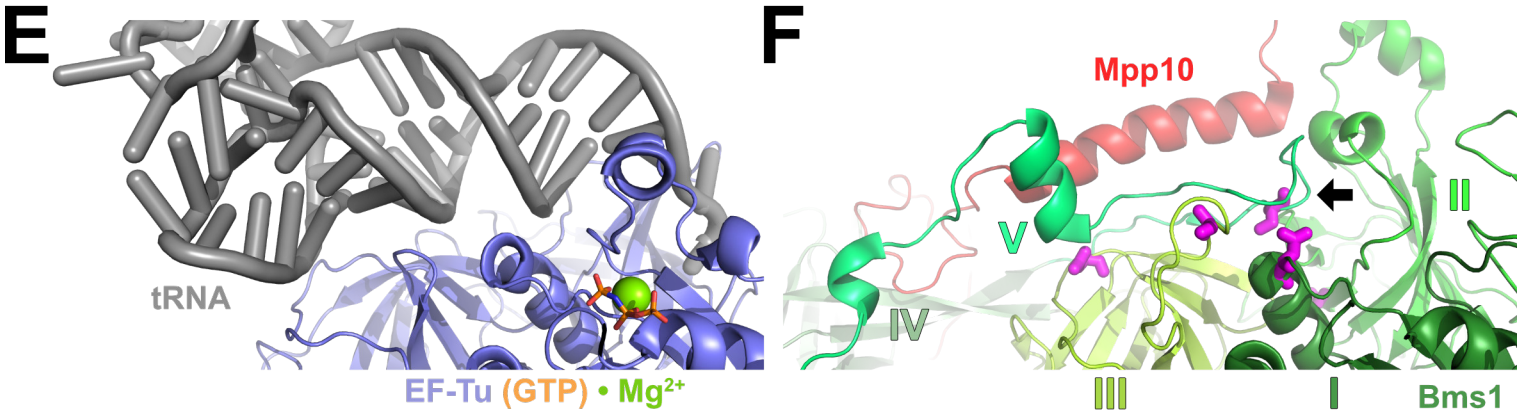

Figure S4, Black, et al 2020

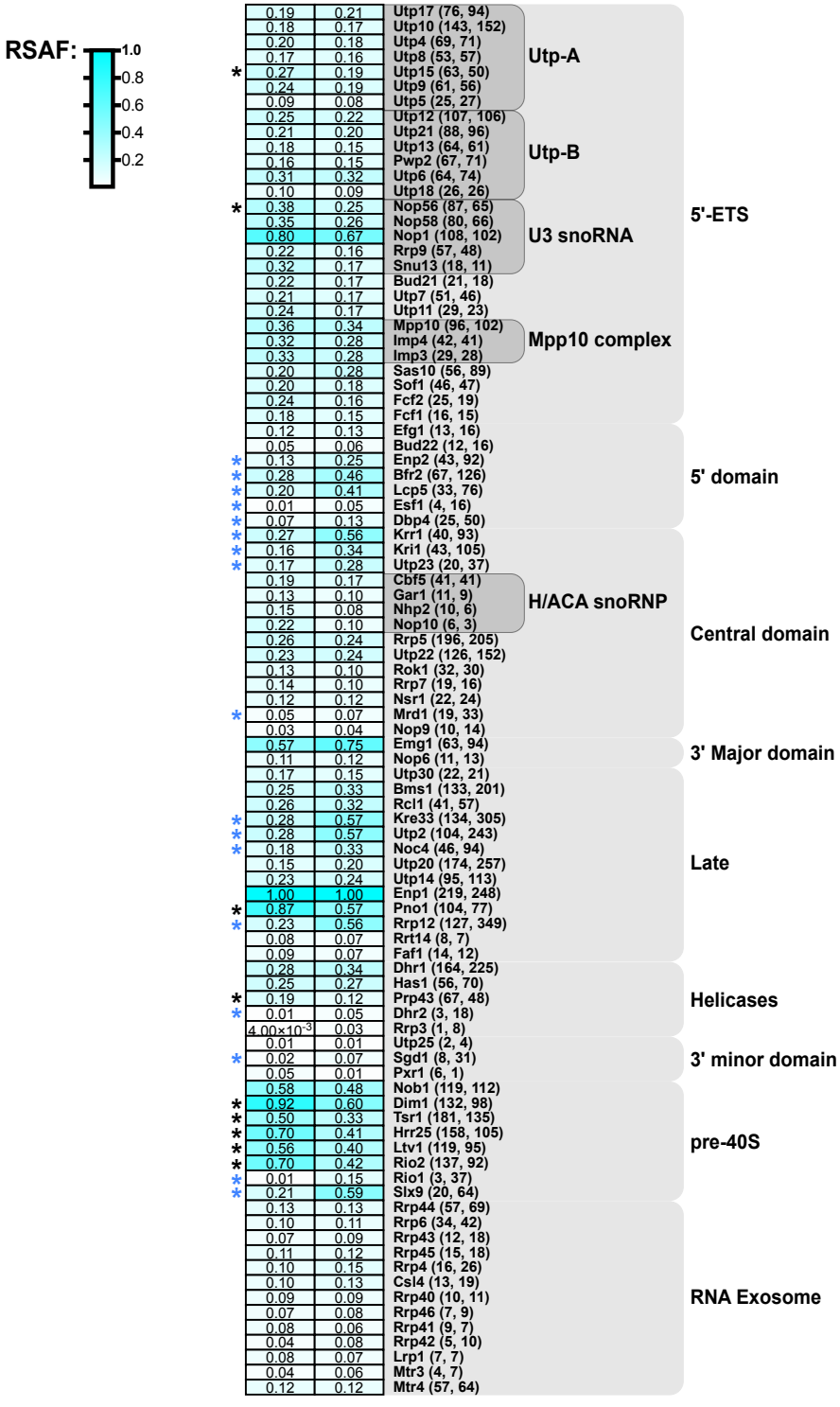

Figure S5, Black, et al 2020

bioRxiv preprint doi: https://doi.org/10.1101/2020.02.05.936237; this version posted February 6, 2020. The copyright holder for this preprint (which was not certified by peer review) is the author/funder. All rights reserved. No reuse allowed without permission.

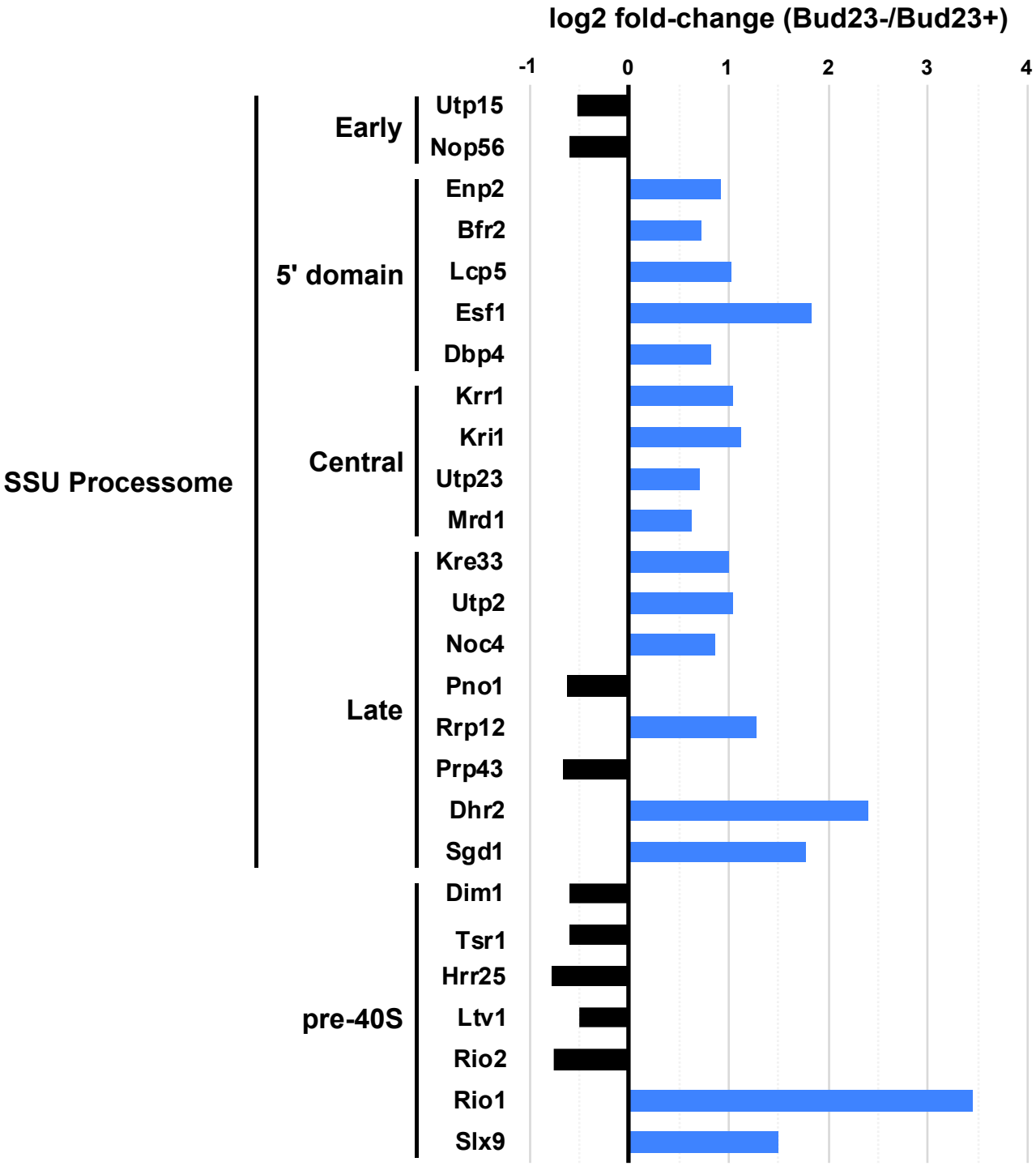

Figure S6, Black, et al 2020